

Predicting the spatiotemporal dynamics of hair follicle patterns in the developing mouse

Chi Wa Cheng^{a,1}, Ben Niu^{a,1}, Mya Warren^{b,1}, Larysa Halyna Pevny^{c,2}, Robin Lovell-Badge^d, Terence Hwa^{b,3}, and Kathryn S. E. Cheah^{a,3}

^aDepartment of Biochemistry, Li Ka Shing Faculty of Medicine, University of Hong Kong, Pokfulam, Hong Kong SAR, China; ^bDepartment of Physics and Center for Theoretical Biological Physics, University of California at San Diego, La Jolla, CA 92093-0374; ^cDepartment of Genetics, University of North Carolina, Chapel Hill, NC 27599; and ^dDivision of Stem Cell Biology and Developmental Genetics, MRC National Institute for Medical Research, London NW7 1AA, United Kingdom

Edited by Stanislav Y. Shvartsman, Princeton University, Princeton, NJ, and accepted by the Editorial Board January 5, 2014 (received for review July 17, 2013)

Reaction–diffusion models have been used as a paradigm for describing the de novo emergence of biological patterns such as stripes and spots. In many organisms, these initial patterns are typically refined and elaborated over the subsequent course of development. Here we study the formation of secondary hair follicle patterns in the skin of developing mouse embryos. We used the expression of sex-determining region Y box 2 to identify and distinguish the primary and secondary hair follicles and to infer the spatiotemporal dynamics of the follicle formation process. Quantitative analysis of the specific follicle patterns observed reveals a simple geometrical rule governing the formation of secondary follicles, and motivates an expansion–induction (EI) model in which new follicle formation is driven by the physical growth of the embryo. The EI model requires only one diffusible morphogen and provides quantitative, accurate predictions on the relative positions and timing of secondary follicle formation, using only the observed configuration of primary follicles as input. The same model accurately describes the positions of additional follicles that emerge from skin explants treated with an activator. Thus, the EI model provides a simple and robust mechanism for predicting secondary space-filling patterns in growing embryos.

Turing pattern | growth and patterns | Voronoi analysis | inhibitory morphogen

In mouse skin development, well defined waves of induction during embryogenesis give rise to several major hair types. The first wave, starting around embryonic day 13 (E13), generates the future guard hair. This primary hair is the longest and is surrounded by Merkel cells (1, 2). The second wave (around E14.5–E16.5) generates two types of secondary hair: awls and auchenes. The third wave (around E17) generates the “Z” shape zigzag tertiary hair. During the formation of these hair types, smaller secondary follicles appear in the interstitial space of the larger primary follicles (1, 3). Unlike the feather buds in chick, which are organized in a highly ordered hexagonal array (4–6), mouse hair follicles are distributed in characteristic but less orderly space-filling patterns, the specifics of which have not been quantitatively characterized (Fig. 1A), and without which a quantitative assessment of pattern integrity in mutants cannot be made.

Turing’s analysis of the reaction–diffusion (RD) model, involving the diffusion of two types of morphogens (“activator” and “inhibitor”) whose interaction regulates their own synthesis, has been regarded as a paradigm to explain the de novo emergence of approximately periodic patterns of epidermal appendages (reviewed in refs. 1, 3, and 7–11; *SI Appendix, Note 1*). The Turing class of RD models were postulated long ago to explain the initiation of skin appendage patterns (8, 12–15), the secondary follicle patterns (16), the coat pattern (17), and skin pigmentation (7, 18, 19). Sick et al. (3) provided molecular evidence for regulators necessary in the formation of hair follicles patterns. They further extended the Turing model developed by Nagorcka and Mooney (8) to describe the patterning of the wave of secondary follicles in between preexisting primary follicles.

However, direct assessment of the applicability of Turing-class models to an observed pattern is difficult due to the lack of quantitative information including the biophysical properties and the initial distribution of the morphogens, all of which can significantly affect quantitative predictions by these models (20).

Equally importantly, the physical growth of the embryo is often not taken into account in typical applications of Turing models. In a number of cases where physical growth was considered, the models were found to generate peak doubling via either tip-splitting bifurcations or tip insertion depending on model parameters and the specifics of the growth kinetics (17, 21–23). Because tip-splitting processes have never been observed in hair follicle development, even qualitative assessment of the applicability of Turing-type RD models to follicle development requires quantitative knowledge of the model parameters, which is difficult. Moreover, existing studies of Turing models with growth have been done in one spatial dimension (24, 25), or on the effective 1D problem of stripe formation in two dimensions (26, 27), but not on the geometrically more complex case of spot formation in 2D.

Here we describe an alternative approach to characterize the formation of secondary hair follicle patterns in the developing mouse, after the establishment of the primary follicles (13). We show quantitative spatiotemporal data for the formation and placement of newly generated hair follicles. These data motivate a simple mathematical model that predicts the timing and location

Significance

The establishment of orderly patterns in living systems is fascinating. While the Turing class of reaction–diffusion models defines a paradigm for the emergence of primary patterns, we propose here a much simpler expansion–induction (EI) model for the formation of secondary patterns. The EI model is derived from a simple geometric rule revealed by quantitative analysis of the patterns of secondary hair follicles in the developing mouse. It is driven by the physical growth of the embryo and is able to predict the formation of secondary follicles spatially and temporally, given only the locations of primary follicles. The robustness of the EI model provides an important advance by allowing comparison to real biological patterns beyond the qualitative, visual level.

Author contributions: C.W.C., B.N., R.L.-B., T.H., and K.S.E.C. designed research; C.W.C., B.N., and M.W. performed research; L.H.P. contributed new reagents/analytic tools; C.W.C., B.N., M.W., and T.H. analyzed data; and C.W.C., B.N., M.W., T.H., and K.S.E.C. wrote the paper.

The authors declare no conflict of interest.

This article is a PNAS Direct Submission. S.Y.S. is a guest editor invited by the Editorial Board.

¹C.W.C., B.N., and M.W. contributed equally to this work.

²Deceased September 30, 2012.

³To whom correspondence may be addressed. E-mail: kathycheah@hku.hk or hwa@ucsd.edu.

This article contains supporting information online at www.pnas.org/lookup/suppl/doi:10.1073/pnas.1313083111/-DCSupplemental.

of newly formed follicles without knowledge of the morphogen profiles or the growth dynamics.

Results

Sox2 Expression Marks the Positions of Primary and Secondary Hair Follicles. Primary and secondary follicles are characterized and distinguished by expression of Sox2 in the dermal papillae and Merkel cells (28) (Fig. 1B). We used the *Sox2* regulatory mutant *Yellow submarine* (*Ysb*) (29), in which the endogenous regulatory elements of *Sox2* that drive its expression in the inner ear and hair follicles control expression of a *LacZ* transgene (29, 30). Thus, *LacZ* expression allows the identification of both the primary and secondary follicles by X-gal staining (Fig. 1A–C), enabling the ensuing analysis of the spatial patterns of the primary (red arrows) and secondary (blue arrows) hair follicles formed at different stages of embryo development (E14.5 in Fig. 1D and E15.5 in Fig. 1G).

Voronoi Analysis Reveals Hidden Regularity in the Spatial Distribution of Hair Follicle Positions. A cursory inspection of the pattern of follicle positions reveals that it is globally disordered, but locally ordered. Therefore, to characterize the spatial arrangement of the secondary follicles relative to the primary follicles in detail, we applied the Voronoi analysis (*SI Appendix*, Fig. S1), which is widely used in characterizing local ordering and has been particularly important in the study of liquids (31). We constructed Voronoi diagrams based on the locations of the primary follicles formed by the *Sox2^{Ysb/+}* embryo at E14.5 (red dots in Fig. 1E), shown as polygons (white lines) surrounding the primary follicles. Each polygon defines the boundaries of a “Voronoi cell,” which partitions the interstitial space into regions located closest to each primary follicle (*SI Appendix*, Fig. S1). Only a small number of secondary follicles (blue dots) were detected at this stage; significantly, all were located close to the vertices of the Voronoi cells.

Next, we analyzed the follicle patterns formed at E15.5 (Fig. 1H), by which time most of the secondary hair follicles were detectable. The same Voronoi analysis based on the positions of the primary follicles (red dots) for 10 such embryos revealed a portion ($46 \pm 8.4\%$, SD) of secondary follicles located on the Voronoi boundaries (vertices and edges). These boundary-located secondary follicles appeared larger than the remainder ($54 \pm 8.4\%$, SD) located in the interior (*SI Appendix*, Fig. S2), suggesting that they had formed earlier (32). We refer to these follicles as IIA follicles and the ones in the interior as IIB follicles (Fig. 1H, blue and orange dots, respectively). Strikingly, if a new Voronoi diagram is constructed based on the locations of both the primary and IIA follicles (Fig. 1I), all of the IIB follicles reside close to the vertices of the new Voronoi cells. A difference between the follicles at E14.5 and E15.5 that will be crucial for the subsequent analysis is that the average areas of the Voronoi cells of the primary follicles increased by nearly threefold (Fig. 1F), indicating increased separation of the follicles due to the physical growth of the embryo. In *Sox2^{Ysb/Ysb}* embryos, there are two copies of the *LacZ* transgene, which show stronger X-gal staining than heterozygotes (Fig. 1J). For the same stage, the enhancement of the signal reveals more juvenile IIB follicles (Fig. 1M), which exhibit a similar pattern as the IIB follicles in *Sox2^{Ysb/+}* embryos; in other words, they reside close to the boundaries of the Voronoi cells formed by the primary and IIA follicles (Fig. 1K and L).

Generation of Secondary Follicles by the Expansion–Induction Model. As illustrated in *SI Appendix*, Fig. S1, vertices of the Voronoi cells are located furthest away from the follicles generating the Voronoi cells. Thus, one possible reason for the initial formation of secondary follicles at the Voronoi vertices (rather than in the much larger interior space) is a tendency for the secondary follicles to form far from the preexisting primary follicles. This pattern

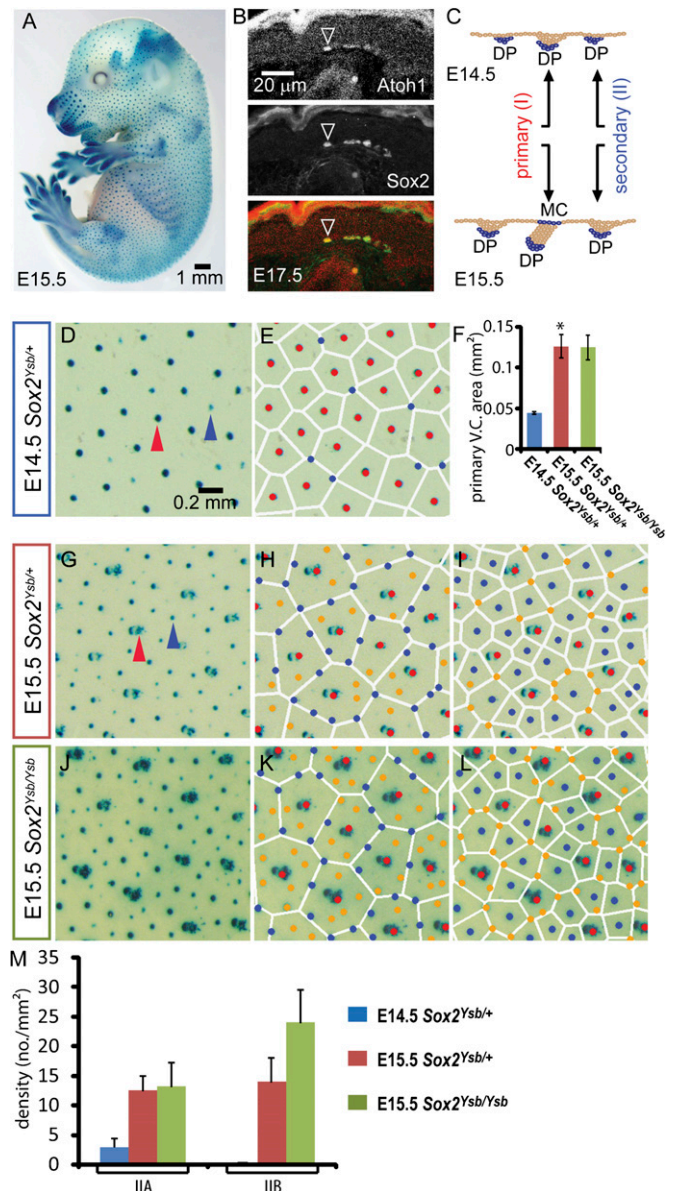


Fig. 1. Spatial regularity in hair follicle patterns as revealed by Voronoi analysis. (A) Whole-mount X-gal staining of an E15.5 *Sox2^{Ysb/+}* mouse embryo. (B) *Sox2* is coexpressed with Merkel cell marker *Atoh1* in E17.5 skin. (C) Schematic diagram of *LacZ* expression in primary and secondary follicles during hair morphogenesis in *Sox2^{Ysb/+}* embryos. At E14.5, the primary and secondary follicles, marked by *LacZ* (X-gal staining) expressed from the dermal papillae (DP), can be distinguished by their relative sizes because secondary follicles (fainter) are just beginning to emerge (blue arrowhead, D). (E) A Voronoi diagram is generated according to the positions of the primary hair follicles (red dots) in E14.5 skin. All secondary follicles (blue dots) are located near the vertices of the Voronoi cells (white polygons). (F) The average area of the Voronoi cells generated by the primary hair follicles. The E15.5 Voronoi cells are ~ 2.8 -fold larger than ($*P < 0.05$) the E14.5 Voronoi cells, indicating expansion of the epithelium during this time. At E15.5, primary follicles are distinguished by the characteristic associated presence of Merkel cells (MC), which also express *LacZ* (red arrowhead in G). (H) The same Voronoi diagram as (E) is generated for E15.5 skin. Two groups of secondary follicles are seen: IIA (blue dots) located close to the Voronoi boundaries, and IIB (orange dots) located in the interior of the Voronoi cells; see Supplemental Methods. (I) A Voronoi diagram generated according to the positions of the primary and IIA follicles. (J) In the *Sox2^{Ysb/Ysb}* E15.5 skin, the X-gal signal is stronger, hence more juvenile IIB hair follicles could be observed (M). (K and L) IIA (blue) and IIB (orange) follicles are distinguished by the Voronoi diagrams as shown in H. (L) Similar to the *Sox2^{Ysb/+}* E15.5 skin, the IIB follicles fall on the vertices of the Voronoi diagrams generated by the primary and IIB follicles.

could occur if each primary follicle produces morphogen molecules that diffuse to the surrounding space and inhibit the formation of secondary follicles. Turnover of the morphogen would ensure that the inhibitory effect is confined to a finite distance ℓ from the primary follicles, given by the distance the morphogen can diffuse before turning over (*SI Appendix, Note 1*). To explain why secondary follicles form initially right at the Voronoi vertices (Fig. 1*E*), we propose a dynamic mechanism driven by the expansion of the skin (Fig. 2). This expansion process is marked by a gradual increase in the distances between the primary follicles (Fig. 1*F*), or the distance d between a Voronoi vertex and the surrounding primary follicles (Fig. 2*A*). Initially, $d < \ell$ for all vertices; the inhibitory zones (green circles) overlap and no secondary follicles could form. As expansion proceeds, there comes a time when the Voronoi vertex becomes no closer than ℓ from any primary follicles, allowing a new follicle to form at the Voronoi vertex. Vertices with successively smaller d will reach the scale ℓ later in the expansion process. We expect the newly

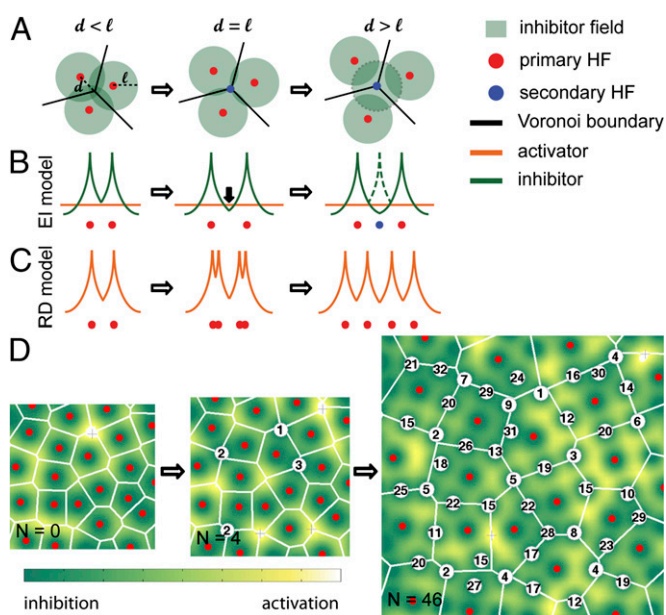


Fig. 2. Generation of secondary follicles by the EI model. (A) Illustration of new follicle induction as a result of epithelial expansion: The three primary follicles (red dots) each synthesize an inhibitor which diffuses to a distance ℓ (green circles). The lines are the edges of the Voronoi cells constructed from the three primary follicles. The vertex (where the three edges meet) is at an equal distance (d) from the three follicles. As the skin expands and the three follicles move away from each other, the vertex is the first location to escape from inhibition (when $d = \ell$) and a new follicle (blue dot) is generated. The inhibitor synthesized by the new follicle (zone indicated by the dashed circle) suppresses the formation of additional follicles in the immediate vicinity as expansion proceeds further. (B) A 1D illustration in terms of the diffusible inhibitor's concentration (green curves) localized to each follicle. In the EI model, a new follicle is created at a location where the local inhibitor concentration falls below a certain level (orange line) and basal activation sets in. Upon formation of the new follicle (blue dot), a new inhibitor field (dashed green line) is immediately established. (C) Turing-type RD model in a continuously expanding domain. Although different types of behaviors are possible depending on the parameter choices, a dominant class of behaviors has the activator concentration (red curve) first bifurcating into two peaks, followed by migration to new quasiequilibrium locations (21). (D) Simulation of new hair follicle formation during expansion according to the EI model. $n = 0$: The initial condition taken from the arrangement of primary follicles. $n = 4$: Shortly after the system started expanding, four new follicles were generated (white circles), each marked by a number indicating its birth time. $n = 46$: The simulation is stopped at a later time when the number of new follicles is 46.

formed follicles to have the same inhibitory zone radius, ℓ . This expectation is based on the fact that IIB follicles are located at the vertices of Voronoi cells generated by the primary and IIA follicles (Fig. 1*I*), which suggests that the primary and IIA follicles exert comparable inhibitory effects on the formation of the IIB follicles. We also expect that once the hair follicle is formed, it becomes insensitive to both activator and inhibitor (3).

The above cartoon scenario can be formulated into a quantitative mathematical model (*SI Appendix, Note 2*), assuming that (i) each existing follicle (primary and secondary) synthesizes inhibitory morphogens, which diffuse and turnover in the interstitial space in the same way; (ii) the follicles are embedded in space which expands uniformly at a constant rate, much slower than the rate of morphogen diffusion and turnover; and (iii) a new follicle is formed at the location where the inhibitory morphogen drops to a certain level below which basal activation takes over. We refer to this model as the expansion–induction (EI) model, as it features the irreversible induction of hair follicle formation when the inhibitor level is lowered due to the physical expansion process (Fig. 2*B*). Unlike Turing models, which use a “short-range activation and long-range inhibition” strategy to generate space-filling patterns, diffusible activators are not required in the EI model as long as there exists a basal level of activity to drive the formation of new follicles for sufficiently low inhibitor levels. [However, the EI model can also accommodate a diffusible activator synthesized from the follicles as long as the activator is longer ranged than the inhibitor; see *SI Appendix, Note 2* and below.] Furthermore, we note that, in the Turing model implementation by Sick et al. (3) using a one-step expansion, the follicles are formed in a single burst rather than sequentially, and their positions do not align well with the Voronoi boundaries as do the observed follicles (*SI Appendix, Fig. S3*). Moreover, previous studies of Turing models on continuously expanding spatial domains found a variety of peak-doubling mechanisms depending on model parameters (21, 22), including tip-splitting bifurcation followed by follicle migration toward the new equilibrium positions (Fig. 2*C*); neither of these processes are consistent with current understanding of hair follicle development. Although peak insertion processes similar to those found for hair follicles can also be generated by Turing models on growing domains (23), the parameter dependence of these models substantially weakens their predictive power compared with that of the EI model described below.

Simulation of New Hair Follicles Formation During Expansion According to the EI Model. Starting with a configuration of primary follicles observed on the E15.5 skin as the initial condition, the EI model inserts secondary follicles sequentially into the interstitial space (Fig. 2*D*; numbers indicate the “birth time” of the corresponding secondary follicles). As expected, the insertion sites were at the Voronoi vertices of the primary follicles at early times, but took up interior positions at later times, after the vertex positions were mostly occupied (*SI Appendix, Fig. S4* and *Movie S1*). Therefore, the EI model provides a simple explanation for the geometric rule exhibited by the IIA and IIB follicles (Fig. 1*E, H, and I*), independent of the activation mechanism or model parameters.

The EI Model Predicts the Position and Timing of Appearance of Secondary Follicles. So far, the comparison between the model output (Fig. 2*D*) and the observed patterns (Fig. 1) is at a static, geometrical level. Next, we describe experiments to test quantitatively various predictions of the EI model, regarding both the location and timing of the new follicles. The analysis was done for the hair follicle pattern from the E15.5 flat-mounted X-gal-stained *Sox2*^{Ysb/+} and *Sox2*^{Ysb/Ysb} skin. In Fig. 3*A*, the observed primary and secondary follicles are shown as the red dots and black circles, respectively. New follicles generated by EI (starting

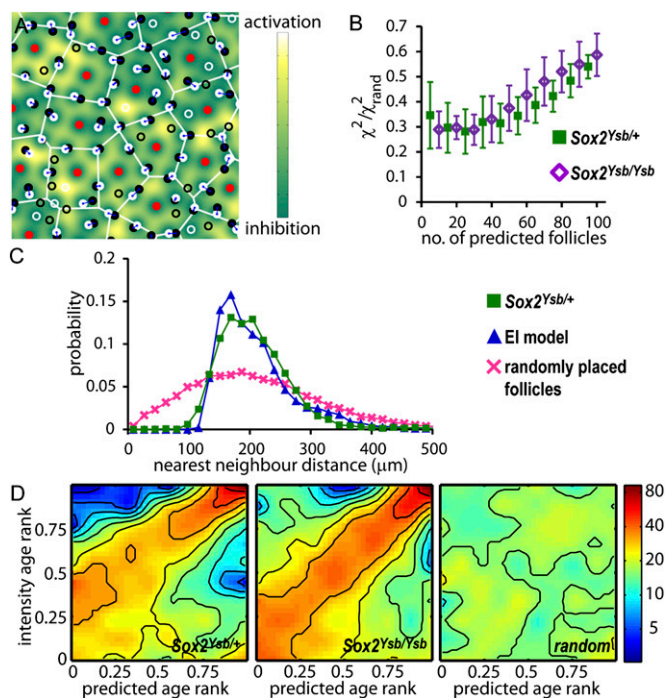


Fig. 3. The EI model predicts the position and timing of appearance of secondary follicles. (A) The locations of the primary follicles (red) are used by the EI model to predict the location of secondary follicles (shown as white circles); the observed secondary follicles are labeled as black circles. If the predicted follicle can be paired with an observed follicle nearby, both follicles are indicated as filled circles and are linked by a line. Unpaired follicles are indicated as open circles. Two follicles are paired if the follicle newly created by the EI model is a mutual nearest neighbor with an unpaired observed follicle, and if the mutual distance is smaller than a specified threshold; see *SI Appendix, SI Materials and Methods*. (B) The root mean square distance, χ^2 , between the predicted follicles and their nearest neighbors among the observed follicles, versus the number of follicles predicted for the $Sox2^{Ysb/+}$ E15.5 skin (solid green squares), and the $Sox2^{Ysb/Ysb}$ E15.5 skin (open purple diamonds). χ^2 is normalized by the limiting value for randomly placed follicles, χ^2_{rand} such that a completely random placement would reach χ^2 value of 1. χ^2 is plotted versus the number of follicles predicted, in the order they appear in the EI model. (C) The probability distribution of the distance between nearest neighbors in the experimental (green squares), predicted (blue triangles), and the random follicle patterns (pink crosses). (D) The age of an observed follicle is estimated as the linear dimension of the follicle size (*SI Appendix, Fig. S2*) and correlates clearly with the birth time of the EI-predicted follicles. Panels show the density of points in the rank ordering of the observed versus predicted follicle ages for the 10 samples of E15.5 skin from $Sox2^{Ysb/+}$ (Left) and $Sox2^{Ysb/Ysb}$ (Center) (*SI Appendix, Fig. S6* and main text). (Right) The distribution for randomly placed predicted follicles on the $Sox2^{Ysb/+}$ E15.5 skins. The correlation can be seen in the broad maximum in density (reddish color) along the diagonal for the observed and predicted follicles, whereas the density is uniform for randomly placed follicles (Right).

with the red dots as the initial follicle pattern) are shown as the white circles. In Fig. 3B, we assess the accuracy of follicle placement in the EI model by first pairing each of the predicted follicles with their nearest neighbor among the observed secondary follicles. The positional error is determined by χ^2 , the root mean squared distance between the observed–predicted pair for the 10 combined samples of the $Sox2^{Ysb/+}$ E15.5 skin (green squares) and the $Sox2^{Ysb/Ysb}$ E15.5 skin (purple diamonds). We normalized the χ^2 values and show a greater than threefold improvement of follicle prediction over the random distribution. χ^2 gradually increases as more follicles are placed, due to the compounded effect of small errors in early follicle placement.

The most significant feature of the follicle pattern is the extremely regular distances between neighboring follicles. In Fig. 3C,

we plot the combined distribution of nearest neighbor follicle distances for the complete pattern of primary plus secondary follicles in the 10 $Sox2^{Ysb/+}$ E15.5 skin samples (green squares). This distribution is sharply peaked at 170 μm , and there are essentially no neighbors at an interfollicle distance of less than 100 μm , which may be interpreted as the minimum inhibitory distance, l . The EI model reproduces the interfollicle distance distribution extremely well (blue triangles), whereas a random distribution of follicle positions gives a much wider distribution (pink crosses), with significantly more follicles that are very close together. For the complete patterns of all neighbor distances for the observed, predicted, and random follicles, see *SI Appendix, Fig. S5*.

Finally, the EI model not only predicts the final pattern of follicle locations, but also the temporal evolution of the pattern. To examine the timing of secondary follicle formation, we hypothesize that the size and intensity of a follicle reflects its age. Next, we pair each predicted follicle with its closest observed follicle (within some reasonable range that excluded <10% of the follicles). The age of each observed and predicted pair is plotted as a point in a correlation plot, with the age taken as a rank ordering; the youngest follicle is assigned an age of one, the next is two, and so on (*SI Appendix, Fig. S6*). The rank-ordered age has the advantage that sample images with different average follicle intensities may be combined together on the same plot. The collage of all of the correlation plots can be quantified as a density plot as shown in Fig. 3D for data obtained from 10 samples each of $Sox2^{Ysb/+}$ and $Sox2^{Ysb/Ysb}$ E15.5 skin. In both cases, despite background arising from a stochastic component to the follicle intensities (*SI Appendix, Fig. S7*), there is clearly a correlation between the predicted and observed ages, as indicated by a maximum in the distribution along the diagonal. In contrast, there is no correlation between the observed follicle age and predicted follicles placed randomly (Fig. 3D, Right). Thus, the EI model is able to predict simultaneously the position and timing of follicle formation, given only the information of the positions of the primary follicles. Similar results are obtained using a diffusible activator instead of basal activation (*SI Appendix, Fig. S8*).

The EI Model Predicts the Position of Additional Follicles Formed in Explant Skins. In the EI model, formation of new hair follicles is driven by the physical expansion of the embryo, which changes the spatial activator/repressor ratio (Fig. 2A and B). However, the model does not require physical expansion if the activator/repressor ratio can be altered independently. To examine the follicle patterns resulting from the latter process, we followed the emergence of new follicles in skin explants from $Sox2^{Egfp/+}$ knock-in reporter mice (13, 33) (Fig. 4A), in which physical expansion is expected to be minimal but the activator/repressor ratio can be manipulated. In these mice, EGFP reports transcription from the *Sox2* locus, allowing us to follow the temporal emergence of these follicles by repeatedly imaging the location of the primary and secondary hair follicles. For E15.25 $Sox2^{Egfp/+}$ back skin, newly emerged follicles can be readily identified after 24 h of culture (T24) by comparisons with the image of the same skin at the beginning of culture (T0) (Fig. 4B and C). On average, ~ 40 EGFP-expressing follicles per mm^2 could be identified at T0, and ~ 16 more emerged at T24 (blue bars, Fig. 4D). During the incubation period, the growth of the hair follicles is clearly seen in the vertical direction (*SI Appendix, Fig. S9*), indicating the viability of the tissue; but there is little or no lateral expansion of the skin in the explant cultures (*SI Appendix, Fig. S10*), as expected (34). Because there is no lateral expansion, many of these newly emerged follicles were likely already pre-specified, but not yet observable, when the fetuses were dissected. The identity of endogenous follicle activator/repressor is still unknown (35). However, exogenous treatment by the BMP antagonist noggin can increase the density of hair follicles in

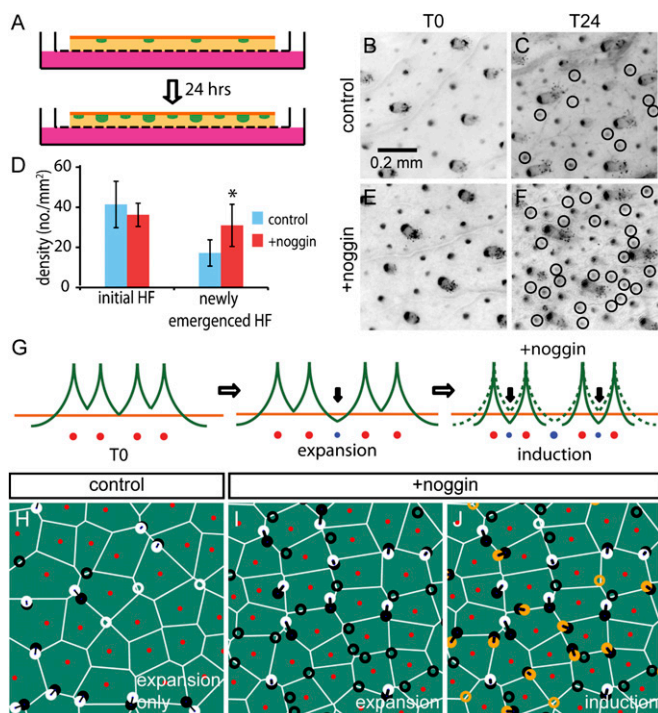


Fig. 4. Modulation of the inhibitor level in explant skins. (A) Schematic diagram of the explant culture. E15.25 *Sox2^{Egfp/+}* skin was flat-mounted on a filter and cultured for 24 h. For noggin-treated samples, 500 ng/mL noggin was added to the medium. (B and C) Hair follicles of the skin explant at the beginning of the culture (T0) and after 24 h (T24). Circles mark all the newly emerged follicles at T24. For noggin-treated samples (E and F), more newly emerged follicles were found after 24 h of culture. (D) Number of the newly emerged follicles at T24 are significantly more in noggin-treated samples ($*P < 0.05$). (G) Schematic diagram of the two-step EI model to simulate follicle formation in noggin-treated samples. Some follicles were first generated by expansion to match the newly emerged follicles in the control, and the remainder are induced by repression of inhibitor levels by noggin, implemented through a reduction in the lateral diffusion range of the inhibitor; see (SI Appendix, Note 3). (H) Comparison of the positions of newly generated follicles (black) and predicted follicles (white circles) in control sample. In noggin-treated samples, predicted follicles were generated by expansion (I, white circles from the first stage of expansion) and induction (J, orange circles from reduced lateral diffusion).

vitro (13, 36, 37) and should effectively increase the activator/repressor ratio if applied in the explant system. We examined whether the flexibility of the EI model and the pattern simulation were able to accommodate the perturbation of the hair follicle density seen in response to exogenous noggin. Noggin treatment resulted in an average of ~ 15 new follicles at 24 h compared with the untreated skin (Fig. 4B red bars, and Fig. 4D–F). To simulate noggin treatment, we applied the EI model using the observed location of the follicles at T0 as input. As illustrated in Fig. 4G, we first applied expansion to generate the $\sim 40\%$ increase in follicle density as observed in the control sample (Fig. 4C and D), assuming that all those newly emerged follicles were prespecified before embryo dissection when physical expansion occurred. Then, we simulated the effect of noggin treatment (“induction” step in Fig. 4G) by reducing the lateral range of the inhibitors (SI Appendix, Fig. S1 and SI Methods). Additional follicles emerged when the inhibitor level in between follicles dropped below that needed to prevent activation (compare the solid and dashed green lines in Fig. 4G). The positions of the simulated follicles obtained from this procedure agree with the observed new follicles to $\chi^2/\chi^2_{\text{rand}} = 0.4 \pm 0.05$, which is comparable to the degree of agreement between simulation

and observation found for the generation of new follicles during normal growth in vivo (Fig. 3B). In fact, the pattern of follicles produced by noggin treatment is remarkably similar to that produced by expansion, a direct result of the form of the EI equations (SI Appendix, Fig. S11) as explained in SI Appendix, Note 2.

Discussion

The skin and its appendages can form complex patterns to meet diverse physiological needs. However, the mechanisms and principles of pattern formation, especially for placement of hair follicles are poorly understood. Previous studies have demonstrated that the balance of activator/repressor levels (3, 13, 37, 38) and genes involved in planar cell polarity (39–42) may participate in patterning. However, for quantitative understanding of the patterning process, one significant hurdle has been the lack of a precise geometrical characterization of the specific patterns formed.

In this study, we establish a simple geometric approach to characterizing the patterns of secondary hair follicles. By analyzing specific patterns on the skin of individual embryos, we reveal a strikingly simple geometrical rule governing the development of secondary follicles in the mouse embryo. This rule is quantified by the proposed EI model, which can predict accurately both the timing and positions of the newly formed secondary follicles in 2D domains in the growing embryo without requiring quantitative knowledge of the physical and biochemical parameters. In addition, the EI model can predict the patterns arising from altered morphogen levels that change follicle density in the absence of physical growth.

Turing’s RD models have been postulated to govern the generation of many biological patterns including those formed by hair follicles. However, the specific patterns generated by these are sensitive to initial conditions, noise, boundary effects, local growth (expansion) rates, and so forth (43). Despite 50+ years of work on the application of these models to biological patterns, success in accounting for the formation of a specific pattern in any individual animal are limited (24, 25, 44, 45). In contrast, the EI model proposed here was able to account for the spatio-temporal development of specific patterns in a nearly parameter-free manner (SI Appendix, Figs. S12 and S13) without the need for sensitive knowledge of initial concentrations, reaction, diffusion rates, and initiation thresholds, all of which are difficult to obtain. Furthermore, the EI model requires only a single diffusing morphogen (an inhibitor) together with a basal activation mechanism, whereas Turing’s RD models require at least two morphogens.

Turing models are designed to address the de novo formation of patterns and are derived from “diffusion-driven instabilities” (9). In contrast, EI does not attempt to address the self-organization of patterns de novo, but may describe a wide range of space-filling patterns in developmental processes after an initial pattern is laid down. Physical expansion of the patterning domain is a critical element of pattern formation in the EI model. Some Turing models have been shown to accommodate growth, in that in some parameter regime the models can also give rise to peak insertion in between existing peaks in growing 1D or quasi-1D domains (24–27). We are currently not aware of reports of spot insertion generated by Turing-type RD models in continuously growing 2D domains; however, one can imagine that an analogous system in 2D will have many more types of behaviors.

An inhibitor-based model was proposed previously in the context of new teeth formation in reptiles (46). However, there, spatial patterning was determined mainly by the teeth movement with respect to the growth zone in a one-dimensional geometry. The EI model also shares some common features with the model of lateral inhibition proposed to explain the formation of microchaetae and bristles in *Drosophila melanogaster* (47, 48).

However, that model uses a different mechanism (contact inhibition), and has a different instability mechanism: competition rather than growth-driven. Indeed, lateral inhibition is commonly discussed in a fixed domain. Like Turing-type RD models, it is used to account for the de novo generation of patterns, not the maintenance of patterns in a growing domain. The EI model directs the embryo to generate new follicles when the local follicle density becomes too low due to physical growth. The EI model provides a simple mechanism to implement an automated “need-based” strategy, which gives the animal a desired density of hair follicles. Moreover, the target hair density can be easily adjusted by changing the basal activation rate or the rate of inhibitor synthesis, thereby providing evolutionary flexibility as physiological demand changes. EI thus provides a robust and yet flexible means of hair density specification after the primary hair follicle pattern is laid down.

- Mann SJ (1962) Prenatal formation of hair follicle types. *Anat Rec* 144:135–141.
- Straille WE (1960) Sensory hair follicles in mammalian skin: The Tylotrich follicle. *Am J Anat* 106:133–147.
- Sick S, Reinker S, Timmer J, Schlake T (2006) WNT and DKK determine hair follicle spacing through a reaction-diffusion mechanism. *Science* 314(5804):1447–1450.
- Jung HS, et al. (1998) Local inhibitory action of BMPs and their relationships with activators in feather formation: Implications for periodic patterning. *Dev Biol* 196(1):11–23.
- Noramly S, Morgan BA (1998) BMPs mediate lateral inhibition at successive stages in feather tract development. *Development* 125(19):3775–3787.
- Lin CM, et al. (2009) Spots and stripes: Pleomorphic patterning of stem cells via p-ERK-dependent cell chemotaxis shown by feather morphogenesis and mathematical simulation. *Dev Biol* 334(2):369–382.
- Baker RE, Schnell S, Maini PK (2009) Waves and patterning in developmental biology: Vertebrate segmentation and feather bud formation as case studies. *Int J Dev Biol* 53(5–6):783–794.
- Nagorcka BN, Mooney JR (1985) The role of a reaction-diffusion system in the initiation of primary hair follicles. *J Theor Biol* 114(2):243–272.
- Turing AM (1952) The Chemical Basis of Morphogenesis. *Philos Trans R Soc Lond B Biol Sci* 237:37–72.
- Kondo S, Miura T (2010) Reaction-diffusion model as a framework for understanding biological pattern formation. *Science* 329(5999):1616–1620.
- Gierer A, Meinhardt H (1972) A theory of biological pattern formation. *Kybernetik* 12(1):30–39.
- Widelitz RB, Chuong CM (1999) Early events in skin appendage formation: Induction of epithelial placodes and condensation of dermal mesenchyme. *J Invest Dermatol Symp Proc* 4(3):302–306.
- Mou C, Jackson B, Schneider P, Overbeek PA, Headon DJ (2006) Generation of the primary hair follicle pattern. *Proc Natl Acad Sci USA* 103(24):9075–9080.
- Närhi K, et al. (2008) Sustained epithelial beta-catenin activity induces precocious hair development but disrupts hair follicle down-growth and hair shaft formation. *Development* 135(6):1019–1028.
- Hughes MW, et al. (2011) In search of the Golden Fleece: Unraveling principles of morphogenesis by studying the integrative biology of skin appendages. *Integr Biol (Camb)* 3(4):388–407.
- Nagorcka BN (1995) The reaction-diffusion (RD) theory of wool (hair) follicle initiation and development. II. Original secondary follicles. *Aust J Agric Res* 46:357–378.
- Othmer HG, Painter K, Umulis D, Xue C (2009) The Intersection of Theory and Application in Elucidating Pattern Formation in Developmental Biology. *Math Model Nat Phenom* 4(4):3–82.
- Kondo S (2002) The reaction-diffusion system: A mechanism for autonomous pattern formation in the animal skin. *Genes Cells* 7(6):535–541.
- Nakamasu A, Takahashi G, Kanbe A, Kondo S (2009) Interactions between zebrafish pigment cells responsible for the generation of Turing patterns. *Proc Natl Acad Sci USA* 106(21):8429–8434.
- Headon DJ, Painter KJ (2009) Stippling the skin: Generation of anatomical periodicity by reaction-diffusion mechanisms. *Math. Model. Nat. Phenom.* 4:83–102.
- Arcuri P, Murray JD (1986) Pattern sensitivity to boundary and initial conditions in reaction-diffusion models. *J Math Biol* 24(2):141–165.
- Crampin EJ, Gaffney EA, Maini PK (2002) Mode-doubling and tripling in reaction-diffusion patterns on growing domains: A piecewise linear model. *J Math Biol* 44(2):107–128.
- Crampin EJ, Gaffney EA, Maini PK (1999) Reaction and diffusion on growing domains: Scenarios for robust pattern formation. *Bull Math Biol* 61(6):1093–1120.
- Economou AD, et al. (2012) Periodic stripe formation by a Turing mechanism operating at growth zones in the mammalian palate. *Nat Genet* 44(3):348–351.

Materials and Methods

Sox2^{Ysb/+} and *Sox2^{Egfp/+}* mouse strains were previously described (29, 30, 33). Mice were maintained within the animal facilities at the University of Hong Kong. All experiments were authorized by licenses from the Hong Kong Government Department of Health, University of Hong Kong Committee on the Use of Live Animals in Teaching and Research. For a detailed description of the whole-mount X-Gal staining, skin organ culture, and computational analysis, see *SI Appendix, SI Materials and Methods*.

ACKNOWLEDGMENTS. We thank Bryan Ho for help with collecting and preparing skin samples; and Reinhard Faessler, Chi-Chung Hui, Herbert Levine, Lei Tang, and Michael Zhang for helpful suggestions. T.H. and R.L.-B. both acknowledge the support of The University of Hong Kong through the Distinguished Visiting Scholar Scheme. This work was supported by Research Grants Council Grants HKU4/05C and HKU7623/12 and University Grants Council of Hong Kong Grant AoE04/04 (to K.S.E.C.). T.H. and M.W. are supported by the US National Science Foundation through the Center for Theoretical Biological Physics (PHY-0822283), and R.L.-B. is supported by the UK Medical Research Council (U117512772).

- Kulesa PM, et al. (1996) On a Model Mechanism for the Spatial Patterning of Teeth Primordia in the Alligator. *J Theor Biol* 180:287–296.
- Painter KJ, Maini PK, Othmer HG (1999) Stripe formation in juvenile *Pomacanthus* explained by a generalized Turing mechanism with chemotaxis. *Proc Natl Acad Sci USA* 96(10):5549–5554.
- Kondo S, Asai R (1995) A reaction-diffusion wave on the skin of the marine angelfish *Pomacanthus*. *Nature* 376:765–768.
- Driskell RR, Giangreco A, Jensen KB, Mulder KW, Watt FM (2009) Sox2-positive dermal papilla cells specify hair follicle type in mammalian epidermis. *Development* 136(16):2815–2823.
- Dong S, et al. (2002) Circling, deafness, and yellow coat displayed by yellow submarine (*ysb*) and light coat and circling (*lcc*) mice with mutations on chromosome 3. *Genomics* 79(6):777–784.
- Kiernan AE, et al. (2005) Sox2 is required for sensory organ development in the mammalian inner ear. *Nature* 434(7036):1031–1035.
- Finney JL (1970) Random Packings and the Structure of Simple Liquids. I. The Geometry of Random Close Packing. *Proc R Soc Lond A Math Phys Sci* 319:479–493.
- Paus R, et al. (1999) A comprehensive guide for the recognition and classification of distinct stages of hair follicle morphogenesis. *J Invest Dermatol* 113(4):523–532.
- Ellis P, et al. (2004) SOX2, a persistent marker for multipotential neural stem cells derived from embryonic stem cells, the embryo or the adult. *Dev Neurosci* 26(2–4):148–165.
- Kashiwagi M, Kuroki T, Huh N (1997) Specific inhibition of hair follicle formation by epidermal growth factor in an organ culture of developing mouse skin. *Dev Biol* 189(1):22–32.
- Huh SH, et al. (2013) Fgf20 governs formation of primary and secondary dermal condensations in developing hair follicles. *Genes Dev* 27(4):450–458.
- Botchkarev VA, et al. (1999) Noggin is a mesenchymally derived stimulator of hair-follicle induction. *Nat Cell Biol* 1(3):158–164.
- Zhang Y, et al. (2009) Reciprocal requirements for EDAR/NF- κ B and Wnt/ β -catenin signaling pathways in hair follicle induction. *Dev Cell* 17(1):49–61.
- Plikus MV, et al. (2011) Self-organizing and stochastic behaviors during the regeneration of hair stem cells. *Science* 332(6029):586–589.
- Chen J, Chuong CM (2012) Patterning skin by planar cell polarity: The multi-talented hair designer. *Exp Dermatol* 21(2):81–85.
- Guo N, Hawkins C, Nathans J (2004) Frizzled6 controls hair patterning in mice. *Proc Natl Acad Sci USA* 101(25):9277–9281.
- Wang Y, Chang H, Nathans J (2010) When whorls collide: The development of hair patterns in frizzled 6 mutant mice. *Development* 137(23):4091–4099.
- Wang Y, Badea T, Nathans J (2006) Order from disorder: Self-organization in mammalian hair patterning. *Proc Natl Acad Sci USA* 103(52):19800–19805.
- Maini PK, Woolley TE, Baker RE, Gaffney EA, Lee SS (2012) Turing’s model for biological pattern formation and the robustness problem. *Interface Focus* 2(4):487–496.
- Yamaguchi M, Yoshimoto E, Kondo S (2007) Pattern regulation in the stripe of zebrafish suggests an underlying dynamic and autonomous mechanism. *Proc Natl Acad Sci USA* 104(12):4790–4793.
- Cho SW, et al. (2011) Interactions between Shh, Sostdc1 and Wnt signaling and a new feedback loop for spatial patterning of the teeth. *Development* 138(9):1807–1816.
- Osborn JW (1971) The ontogeny of tooth succession in *Lacerta vivipara* Jacquin (1787). *Proc R Soc Lond B Biol Sci* 179(56):261–289.
- Axelrod JD (2010) Delivering the lateral inhibition punchline: It’s all about the timing. *Sci Signal* 3(145):pe38.
- Cohen M, Georgiou M, Stevenson NL, Miodownik M, Baum B (2010) Dynamic filopodia transmit intermittent Delta-Notch signaling to drive pattern refinement during lateral inhibition. *Dev Cell* 19(1):78–89.

Supporting Appendix

Supplementary notes

Note 1: The Turing Model of pattern formation.

Diffusion-driven instability is a canonical mechanism invoked to explain the emergence of space-filling patterns from an initially homogeneous condition (1-3). In the simplest case, the system is constituted of two diffusible and reactive substances (the morphogens). One of them is an activator; it stimulates the production of itself as well as its antagonist, the inhibitor. The inhibitor represses the production of the activator. Both the activator and the inhibitor have finite life times. It was pointed out by Turing (2) that a homogeneous state of this system is unstable, in the sense that any random fluctuation will get amplified and develop into spatially structured patterns, if certain criteria of the kinetic properties of the morphogens are satisfied. These criteria are commonly known as “short-range activation and long-range inhibition”. Typically, they are realized by having activators that are either short lived and/or slow diffusing (or inhibitors that are long lived and/or fast diffusing), such that the synthesis of activators and inhibitors only occur in localized neighborhoods (e.g., spots or stripes). The exact location of spots or stripes depends on small fluctuations in the activator and inhibitor concentrations in the initial condition, and is typically not predictable in advance.

Note 2: The Expansion-Induction Model.

The simplest formulation of the EI model is for a single diffusing inhibitor and basal activation (Fig. 2B). We give a continuum formulation here for the sake of compactness. The discrete numerical implementation is given in the Supplementary Methods section (below).

Let the concentration of the inhibitor in the two-dimensional space $\vec{r} \in (x, y)$ be $R(\vec{r}, t)$, with diffusion coefficient D_R , turnover rate μ_R . Then, the temporal evolution of the inhibitor field is described by the following equation

$$\frac{\partial R(\vec{r}, t)}{\partial t} = D_R \nabla^2 R(\vec{r}, t) - \mu_R R(\vec{r}, t) + \gamma_R(\vec{r}, t) - \nabla \cdot (R(\vec{r}, t) \vec{v}(\vec{r}, t)) \quad (1)$$

where $\gamma_R(\bar{r}, t)$ is the inhibitor synthesis rate. We assume inhibitor synthesis is localized to the positions of the existing follicles. Let the position of the n^{th} follicle be \bar{r}_n and its birth time be t_n , then the inhibitor synthesis function is given by

$$\gamma_R(\bar{r}, t) = \gamma_{R,0} \cdot a^2 \cdot \sum_{n=1}^{N(t)} \delta(\bar{r}(t) - \bar{r}_n(t)), \quad (2)$$

where δ is the Dirac delta function, $N(t)$ is the total number of follicles at time t , a is a microscopic cutoff length (spatial resolution), and $\gamma_{R,0}$ is the rate of inhibitor synthesis by one follicle, assumed to be the same for all follicles regardless of their birth time.

Tissue dilation is included in the changing locations of the follicles, and in the final term in Eq. (2), which gives dilution and convection due to expansion. Dilation is easier to understand if Eq. (2) is made dimensionless. The range of the diffusible inhibitor sets the length scale of the problem:

$$X_R = \sqrt{D_R / \mu_R}. \quad (3)$$

The relevant time scale is

$$T_0 = 1 / \varepsilon, \quad (4)$$

where ε is the tissue expansion rate; and the concentration scale is

$$R_0 = \gamma_{R,0} a^2 / D_R. \quad (5)$$

This is the peak inhibitor concentration at the follicle, set by the balance of the local synthesis rate and diffusion of the inhibitors. The dimensionless equation is then

$$\left(\frac{\varepsilon}{\mu_R} \right) \left(\frac{\partial \tilde{R}}{\partial \tilde{t}} + \nabla \cdot (\tilde{v} \tilde{R}) \right) = \nabla^2 \tilde{R} - \tilde{R} + \sum_{n=1}^{N(\tilde{t})} \delta(\tilde{r}(\tilde{t}) - \tilde{r}_n(\tilde{t})), \quad (6)$$

where $\tilde{R}(\tilde{r}, \tilde{t}) = R(\bar{r}, t) / R_0$, $\tilde{r} = \bar{r} / X_R$, $\tilde{t} = \varepsilon t$, $\tilde{v} = \bar{v} / X_R \varepsilon$. In the following equations, the tilde has been dropped for clarity. If we make the reasonable assumption that $\mu_R \gg \varepsilon$, i.e., the diffusion of the morphogens occur at a much faster time scale than tissue expansion, then we need only to solve

$$\nabla^2 R - R + \sum_{n=1}^{N(\tilde{t})} \delta(\tilde{r}(\tilde{t}) - \tilde{r}_n(\tilde{t})) = 0 \quad (7)$$

to find $R(\bar{r}, t)$ at each time point. In cases where the expansion rate and turnover rate are more similar, the full reaction diffusion equation may be solved using standard numerical approaches. This form of the equation permits a simple solution in the form of a sum over $G(\bar{r}|\bar{r}_n)$ for each follicle position, $\bar{r}_n(t)$:

$$R(\bar{r}, t) = \sum_{n=1}^{N(t)} G(\bar{r}|\bar{r}_n(t)), \quad G(\bar{r}|\bar{r}_n) = \frac{K_0(|\bar{r} - \bar{r}_n|)}{2} \quad (8)$$

where $G(\bar{r}|\bar{r}_n)$, the Green's function of Eq. (7), is the second modified Bessel function, indicated by K_0 above.

The tissue expansion manifests in Eq. (7) through the changing follicle positions $\bar{r}_n(t)$; however, it is actually most easily implemented numerically by having fixed follicle locations, changing instead the extinction length l_R of the Green's function with growth. In this case:

$$G(\bar{r}|\bar{r}_n, t) = \frac{1}{2} K_0 \left(\frac{|\bar{r} - \bar{r}_n|}{l_R(t)} \right), \quad l_R = \frac{X_R}{1+t}. \quad (9)$$

Expansion causes the inhibitor concentration to decrease everywhere. To generate new follicles, we impose the rule that if the inhibitor concentration at some point \bar{r}^* drops to a threshold level R^* at time t^* , then, a new follicle is created at position \bar{r}^* with birth time being t^* , i.e.,

$$N(t^*) = N(t^* - \delta t) + 1 \quad \text{if } R(\bar{r}^*, t^*) \leq R^* \quad (10)$$

with $\bar{r}_{N(t^*)} = \bar{r}^*$, $t_{N(t^*)} = t^*$

The newly created follicles immediately contribute to the synthesis of inhibitors according to Eq. (2), such that no more follicles are created in the immediate vicinity of \bar{r}^* . This rule simulates the action of a basal level of activator for follicle induction, which is suppressed by the inhibitor until it falls below the threshold. Within our model, this threshold (in dimensionless units) represents the only chemical parameter that can affect the pattern secondary follicles formed relative to the primary follicles. The reaction-diffusion and growth parameters are

necessary only if the absolute spatial and temporal dimensions are desired, in which case they can be constrained through fits to the data.

In the discrete simulation of the above system (described in Supplementary Methods), a finite δt means that there is often an extended region in space where the condition $R(\vec{r}^*, t^*) \leq R^*$ is satisfied. To choose new follicle locations without taking too small a time step, we first place a follicle at the global minimum of $R(\vec{r}, t) < R^*$. The inhibitor concentration is recalculated with the new follicle, and the procedure is repeated until R is everywhere above the threshold. At this point, time is advanced again.

Finally, the EI model does not require there be only a diffusible inhibitor with a constant level of (basal) activation. It can also accommodate the case where the activator is diffusible and synthesized by the existing follicles. The activator concentration $A(\vec{r}, t)$ can be determined in the same way as the repressor above. There is a new characteristic length scale $X_A = \sqrt{D_A / \mu_A}$ and production rate $A_0 = \gamma_{A,0} a^2 / D_A$, which appear in the Green's function for the activator

$$G_A(\vec{r} | \vec{r}_n, t) = \frac{A_0}{2R_0} K_0 \left(\frac{|\vec{r} - \vec{r}_n|}{l_A} \right), \quad l_A = \frac{X_A}{X_R} l_R. \quad (11)$$

With a diffusible activator, the rule for new follicle formation may be generalized to, e.g.,

$$\begin{aligned} N(t^*) &= N(t^* - \delta t) + 1 \\ \text{with } \vec{r}_{N(t^*)} &= \vec{r}^*, \quad t_{N(t^*)} = t^* \end{aligned} \quad \text{if } \frac{R(\vec{r}^*, t^*)}{A(\vec{r}^*, t^*)} \leq \theta \quad (12)$$

where θ is the threshold level of the inhibitor-activator ratio. The key criterion for pattern formation in the case of the diffusible activator is that the activator should act over longer range than the inhibitor, i.e.,

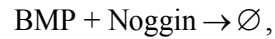
$$X_A = \sqrt{D_A / \mu_A} > X_R = \sqrt{D_R / \mu_R}. \quad (13)$$

In the discrete simulation, the new follicle is created at the local minimum of $R(\vec{r}, t) / A(\vec{r}, t)$.

Note 3: The effect of noggin treatment in explant culture.

Noggin is a homodimeric glycoprotein with high affinity for Bmp2 and Bmp4 and with varying affinities for Bmp5, Bmp6, Bmp7, GDF5 and GDF6, but apparently not other members of the TGF- β family of peptides (4-6). Noggin acts by binding these Bmps directly and prevents their interaction with cell surface receptors (6).

We model the inhibitory effect of Noggin on the inhibitor BMP as a reaction



where \emptyset means an inert product. Denote the rate of the reaction by $\delta(\text{Noggin})$; its effect on follicle pattern formation can be modeled as an effective rate removing the active BMP, with the turnover rate μ_R in Eq. (1) replaced by $\mu_R + \delta(\text{Noggin})$. This amounts to reducing the range of the diffusible inhibitor, X_R , via Eq. (3). To simulate the effect of Noggin treatment (Fig. 4J), we simply decreased X_R to some smaller values and observed the emergence of the follicles. As discussed previously, we expect this to be functionally equivalent to actually expanding the size of the grid.

SI Materials and Methods

Histology and Immunostaining.

Back skin from murine embryo was fixed in 4% paraformaldehyde, cryo-protected, embedded and sectioned at 14 μm . Primary antibodies and dilution were: rabbit anti-Atoh1(7) (1:200), goat anti-SOX2 (Neuromics, 1:600) and rabbit anti- β -galactosidase (Cappel, 1:2000).

Whole-mount X-gal staining.

Whole-mount X-gal staining for detection of β -galactosidase activity was performed as previously described(8) and the X-gal stained embryo was post-fixed in 4% paraformaldehyde. The dorsal skin was dissected out and flat-mounted for imaging by Leica MZFLIII stereo-microscope.

Skin organ culture and treatment.

E15.25 embryonic back skin explants were dissected and cultured for 24 hr on Millicell filters (Millipore) at 37°C in DMEM with 5% FCS, and 100 units/mL penicillin/ streptomycin. For experiments involving treatment of with noggin, 500 ng/mL of noggin (R&D system) was added to the culture medium.

Computational analysis

Identification of follicles and their intensities (ages).

To identify the follicles, we first transformed the 960×960 sample images in RGB color code to the single channeled Grayscale format with pixel values of intensity ranging from 0 to 255. We then performed the binarization transform through Otsu's method (9-12) to convert the Grayscale images to 0-1 matrices in which 1s represent the pixel elements that are positive of X-gal staining signals while 0s represent the non-follicle regions. To locate each individual follicle, we applied local Greedy Searching and Clustering algorithm (13) to determine the linear consecutive regions that contain follicle pixels only (locality cutoff = 4 pixels). The center of the follicle in the sample image matrix can thus be determined by calculating the average of the indices for the member pixel elements in each cluster.

Primary follicles at E15.5 day have developed the bipartite structure characterized by the expression of Sox2 in Merkel cells and the dermal papilla. We used this characteristic association with Merkel cells to identify the epithelial location of the primary hair follicles and developed a computer program tool that allows interactive manual detection and localization of primary follicles. The centers of primary follicles were labeled and recorded with respect to the Merkel cells in the sample images.

To quantify the birth time/ age of each individual follicle that has been identified, we made use of its intensity profile by staining and performed parametric fitting to a 2-dimensional Gaussian shape characterized by the Gaussian widths σ_x and σ_y and an amplitude. We performed the optimization by employing the Steepest Gradient Descent method (14) to minimize the error function of residue differences between the model and the intensity profile of

the follicle. The optimal parameters of the Gaussian model were obtained after the optimization procedure converged to the global minimum of the error function with the best fitting. The size of the follicle reflecting its observed age can thus be estimated as $\sqrt{\sigma_x^2 + \sigma_y^2}$.

Voronoi Analysis.

We employed the incremental method (15) to generate the Voronoi diagrams based on the locations of the hair follicles in $Sox2^{Ysb/+}$ and $Sox2^{Ysb/Ysb}$ samples. For instance, in order to generate the Voronoi diagram for primary follicles, we performed triangulation first on the primary anchor points following the rule of ‘empty circumvent circles’ (16). Therefore, the triangles with the primary follicles on the vertex nodes were optimized to have uniform and regular shapes and sizes. The bisecting lines perpendicular to the edges of these triangles were then drawn and connected to generate the dual map of the triangulation, i.e. the Voronoi diagram with the primary follicles set at the center.

Classification of secondary hair follicles.

The hair follicles that are located on the boundaries of the Voronoi diagrams of the primary follicles were classified as IIA follicles (distance to boundary less than twice of the average of diameters of non-primary follicles i.e. $\sim 70 \mu\text{m}$). The remaining secondary follicles were classified as IIB follicles.

The IIA hair follicles were further classified into 2 groups i.e. the vertex and the edge follicles. The criterion to make this classification is determined by the ratio of distances between the projected point of the hair follicle and the middle point of its closest edge. If the projected point is more than 1.5-fold closer to the vertex than to the middle point then it is classified as being a vertex follicle, otherwise an edge follicle, as illustrated in SI Appendix; Fig. S14.

Simulation of the EI model.

We performed the simulation of the diffusible inhibitor model defined by Eqs. (8)-(10) on a discrete lattice. Two different methods of expansion were explored. In the first, the decay length of the Green’s function is decreased with time using Eq. (9). In the second, the size of the grid is gradually expanded from an initial size of 120×120 until a final size of 480×480 using

$$L(t) = L_i \cdot \left(1 + \frac{t \cdot (L_f - L_i)}{L_i \cdot T} \right), \quad (14)$$

where $L_i = 120$ is the initial grid size, $L_f = 480$ is the final grid size, $L(t)$ is the grid size at the current time t , and $T = 300$ is the total time of simulation. The two methods give statistically identical results (SI Appendix; Fig. S11).

At each time step, we evaluated the inhibitor concentration field $R(\vec{r}, t)$ by simply summing the Green's functions (Eq. 9) for each of the current follicle locations. The initial value of l_R was chosen such that $R(\vec{r}, t)$ is nowhere below the threshold, and then decreased linearly in time. At the boundaries, we have incomplete information about the inhibitor concentration, therefore we only expect accurate follicle prediction inside of a buffer region of twice l_R^* , which is the extinction length where new follicle locations are first identified. A hair follicle is generated at the global minimum of $R(\vec{r}, t)$ if $R < R^*$ with $R^* = 0.1$ being a pre-specified threshold. This event is then added to the list of follicle position \vec{r}_n and birth time t_n .

In case of a diffusible activator, we calculate the activator concentration as well. We used $A_0 / R_0 = 0.4$ and $X_A / X_R = 1.5$ so that the inhibitor is dominant at short scale, but the activator is longer ranged. After each step of expansion and evaluation, we searched in the grid for the positions where the R/A ratios are minimum. We generated a hair follicle at each local minimum position where $R/A < 0.1$.

To simulate the noggin treatment, we used the hair follicles present in T0 as input (Fig. 4E). First, we employed the EI model with the expanding mesh to generate the same number of hair follicles as those detected in controls, i.e., 40% addition of the starting number of follicles at T0 (Fig. 4I). We then stopped expansion and reduced the inhibitor diffusion range, to simulate the effect of noggin on BMP (see Supp Note 3). As noted above, grid expansion and inhibitor range compression are functionally identical in the EI model, thus we see that the noggin treatment leads to qualitatively similar patterns to those produced by growth alone.

Evaluation of spatial and temporal predictions by the EI model.

We selected a portion of the central area of the sample images for evaluation as follicles may be wrongly generated in the regions near the boundary of the simulation domain. We dropped a

boundary region of 50 pixels in width from the full sized area of 480x480. The boundary region is just larger than the minimum distance between primary follicles, which is 40 pixels. Thus, the domain being evaluated is 380x380 in pixel units.

The predicted follicles are paired with their nearest neighbor. Note that observed follicles can be paired with more than one predicted follicle, and this becomes more and more likely as the number of predicted follicles increases. The mean squared distance between the predicted and observed follicles, normalized by the same measurement for the null model where follicles are placed at random, is used to evaluate the strength of the EI model predictions:

$$\frac{\chi^2}{\chi^2_{rand}} = \frac{\left\langle \left(\bar{r}_{pred} - \bar{r}_{obs} \right)_{EI}^2 \right\rangle}{\left\langle \left(\bar{r}_{pred} - \bar{r}_{obs} \right)_{rand}^2 \right\rangle}. \quad (15)$$

We also use this measure to determine the robustness of the EI simulations (below).

Robustness of the results.

The relevant parameters for the EI model are the threshold value of R^* (or θ), the time step, and the grid size. We can also explore the effect of different functional forms for $G(\bar{r}|\bar{r}^*)$, which can arise from possible deviation of morphogen dynamics from the ideal diffusive behavior assumed in Eq. (9). SI Appendix; Fig. S12 shows that the EI model is remarkably robust to the choice of all these parameters and functions. This reflects the essentially geometric nature of the EI model.

We also explore the effect of initial conditions on the model predictions. The only initial condition in the model is the location of primary follicles. Occasionally, smaller primary follicles are misidentified as secondary follicles. To investigate the effect of such an error, we randomly change some identified primary follicles to secondary follicles in one pattern. SI Appendix; Fig. S13A shows the positional error in the predicted follicles given different numbers of primary follicles (legend). The error in the predictions increases very gradually at first, but becomes more severe when 20% of the primary follicles are misidentified. SI Appendix; Fig. S13B shows that the errors in the predicted follicle locations are localized to a region directly surrounding the missing follicle. Additionally, in many cases, the EI model correctly places a secondary follicle very near the missing primary follicle. We conclude that the EI model predictions are remarkably

robust to error in the initial conditions as well.

Supplementary references

1. Headon, D. J. & Painter, K. J. (2009) Stippling the skin: Generation of anatomical periodicity by reaction-diffusion mechanisms. *Math. Model. Nat. Phenom.* **4**, 83-102.
2. Turing, A. M. (1952) The Chemical Basis of Morphogenesis. *Philos. Trans. R. Soc. London B Biol. Sci.* **237**, 37-72.
3. Gierer, A. & Meinhardt, H. (1972) A theory of biological pattern formation. *Biol. Cybern.* **12**, 30-39.
4. Chang, C. & Hemmati-Brivanlou, A. (1999) Xenopus GDF6, a new antagonist of noggin and a partner of BMPs. *Development* **126**, 3347-3357.
5. Merino, R., Macias, D., Galian, Y., Economides, A. N., Wang, X., Wu, Q., Stahl, N., Sampath, K. T., Varona, P., & Hurler, J. M. (1999) Expression and Function of Gdf-5 during Digit Skeletogenesis in the Embryonic Chick Leg Bud. *Developmental Biology* **206**, 33-45.
6. Zimmerman, L. B., De Jesus-Escobar, J. M., & Harland, R. M. (1996) The Spemann Organizer Signal noggin Binds and Inactivates Bone Morphogenetic Protein 4. *Cell* **86**, 599-606.
7. Helms, A. W. & Johnson, J. E. (1998) Progenitors of dorsal commissural interneurons are defined by MATH1 expression. *Development* **125**, 919-928.
8. Leung, K. K. H., Ng, L. J., Ho, K. K. Y., Tam, P. P. L., & Cheah, K. S. E. (1998) Different cis-Regulatory DNA Elements Mediate Developmental Stage- and Tissue-specific Expression of the Human COL2A1 Gene in Transgenic Mice. *J. Cell Biol.* **141**, 1291-1300.
9. Baltus, A. E., Menke, D. B., Hu, Y. C., Goodheart, M. L., Carpenter, A. E., de Rooij, D. G., & Page, D. C. (2006) In germ cells of mouse embryonic ovaries, the decision to enter meiosis precedes premeiotic DNA replication. *Nat. Genet.* **38**, 1430-1434.
10. Otsu, N. (1979) A threshold selection method from gray level histograms. *IEEE Trans. Sys. , Man. , Cyber.* **9**, 62-66.
11. Lutes, A. A., Neaves, W. B., Baumann, D. P., Wiegraebe, W., & Baumann, P. (2010) Sister chromosome pairing maintains heterozygosity in parthenogenetic lizards. *Nature* **464**, 283-286.
12. Wang, Y., Botvinick, E. L., Zhao, Y., Berns, M. W., Usami, S., Tsien, R. Y., & Chien, S. (2005) Visualizing the mechanical activation of Src. *Nature* **434**, 1040-1045.

13. Gdalyahu, Y., Weinshall, D., & Werman, M. (2001) Self-organization in vision: Stochastic Clustering for Image Segmentation, Perceptual Grouping and Image Database Organization. *IEEE Trans. on Pattern Analysis and Machine Intelligence* **23**, 1053-1074.
14. Nocedal, J. & Wright, S. J. (2006) *Numerical Optimization* (Springer-Verlag, Berlin, New York).
15. Hjelle, O. & Daehlen, M. (2006) (Springer, Berlin Heidelberg), pp. 1-21.
16. Okabe, A., Boots, B., Sugihara, K., Chiu, S. N., & Kendall, D. G. (2000) in *Spatial Tessellations* (John Wiley & Sons, Inc., pp. 43-112.
17. Sick, S., Reinker, S., Timmer, J., & Schlake, T. (2006) WNT and DKK Determine Hair Follicle Spacing Through a Reaction-Diffusion Mechanism. *Science* **314**, 1447-1450.

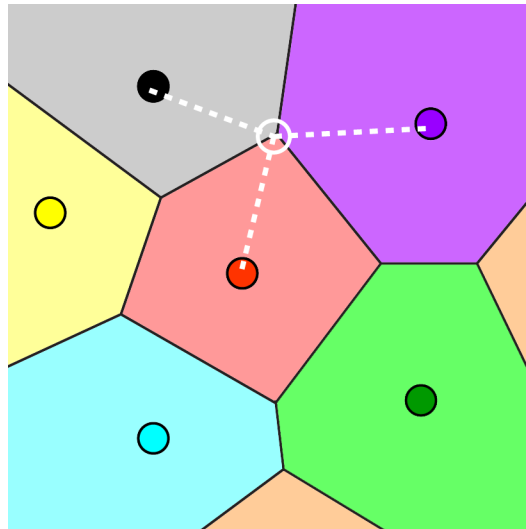


Fig. S1: Voronoi analysis. Voronoi tessellation is mathematical method widely used in the analysis of spatial structures (13). Given a set of N anchor points in 2-dimensional space, a Voronoi diagram is generated by subdividing the space into N non-overlapping polygons (called the “Voronoi cells”) such that all points inside a cell have the shortest distances to the anchor point of that cell than any other anchor points. In the above figure, the anchor points are the colored circles, and the Voronoi cells are the colored regions bordered by the black lines (called the “Voronoi edges”). All points inside a colored region are closer to the circle of the same color than to any other circles. A property of the Voronoi cells important for the present study is that a Voronoi vertex, defined by the intersection of typically 3 Voronoi edges and illustrated by a white open circle, is at an equal distance from the three surrounding anchor points (white dash lines), and any points in the vicinity of the vertex will be closer to at least one of the anchor points.

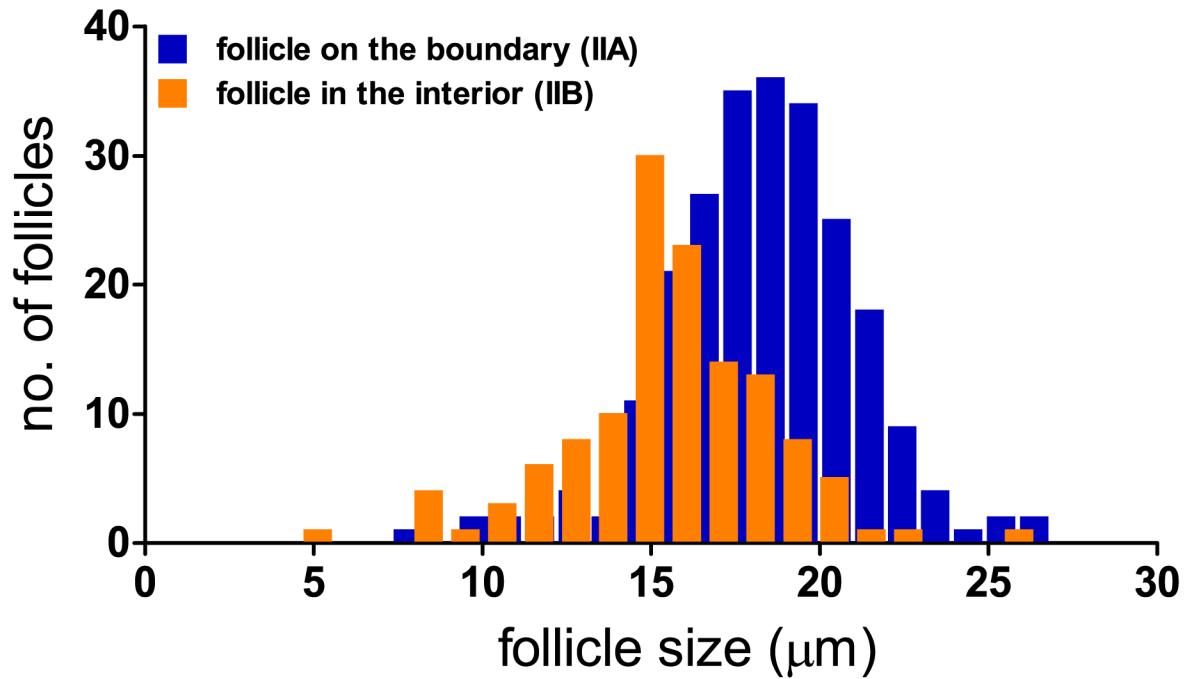


Fig. S2: Follicles located in the interior of Voronoi cells have younger ages than follicles at the boundary. We assume the size of the follicles reflect their ages and analyzed the follicle sizes. The spatial distribution of X-gal stain intensity of each identified secondary follicle is fitted to a 2-dimensional Gaussian function parameterized by two widths, σ_x and σ_y , and the “size” of the follicle is defined as $\sqrt{\sigma_x^2 + \sigma_y^2}$; see *SI Materials and Methods* Computational analysis for details. Data were collected for the secondary follicles on the E15.5 skins and sorted into two groups, according to whether they are located on the boundaries (IIA) or in the interior space (IIB) of the Voronoi cells generated from the primary follicles; see Fig. 1G. Size distribution of the IIA (blue) and IIB (orange) follicles show that the average size of the IIA follicles is 18.3 μm and the IIB follicles is 15.6 μm ($n=3$). Thus, we expect the IIA follicles to form somewhat than the IIB follicles. However, this temporal order is not expected to be very sharp according to the simulation result of SI Appendix; Fig. S4, thus explaining the substantial overlap of the two distributions.

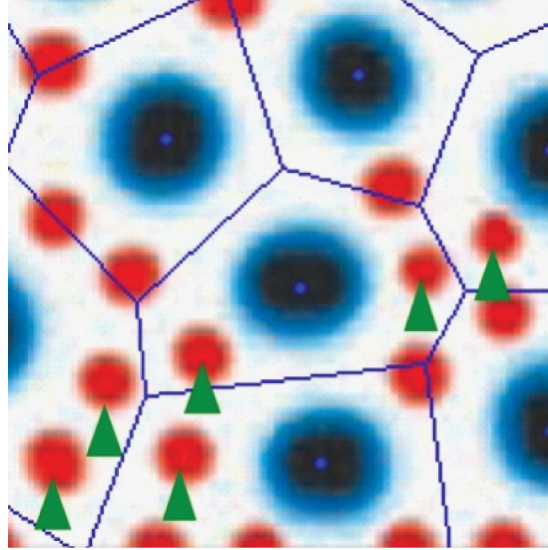


Fig. S3: Voronoi analysis of the computational result of Sick et al (17). In Ref(17), two waves of hair follicles were generated by first using a Turing RD model to generate the primary follicles, followed by a spatial expansion, and another round of RD model to generate the secondary follicles in the interstitial space of the primary follicles (which are held fixed in the study once generated by the first RD run). Clearly, the secondary follicles generated this way all appear around the same time instead of the sequential appearance predicted by the EI model. The spatial positions of the newly generated follicles are also different from those of the EI model. The figure above shows the predictions of Sick *et al*'s model, with the blue and red dots being the primary and secondary follicles respectively, superimposed with the Voronoi cells generated from the primary follicles. While many follicles fall on the Voronoi boundaries, there are also substantial numbers of follicles that do not adhere to the Voronoi boundaries. For example, in the regions indicated by the green arrows, the red follicles essentially fill up the open space with a preferred spacing without regard to the Voronoi boundaries. Moreover, the preferred spacing is highly parameter dependent, such that denser filling of the interstitial space can be easily arranged by, e.g., reducing the scale of the diffusion zone (ℓ). Thus, the patterns generated by the Turing RD model are sensitively dependent on the model parameters.

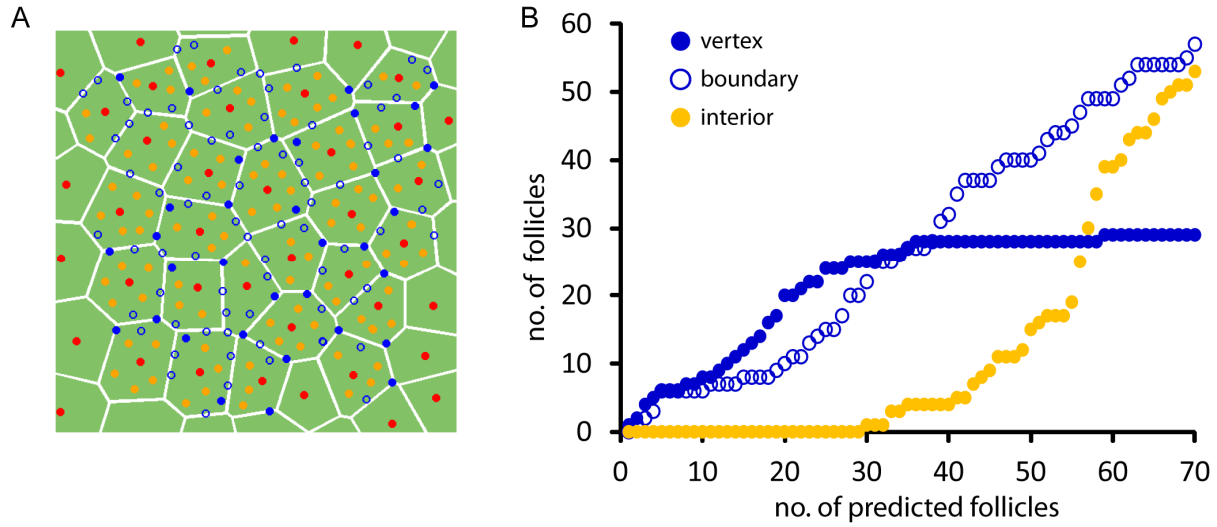


Fig. S4: Positions of the inserted secondary follicles. (A) Follicles generated by the EI model are classified into one of the three types according to their positions close to the vertices (solid blue), edges (open blue), and the interiors (orange) of the Voronoi cells generated according to the positions of the primary follicles (red). (B) The total number of each of these classes of new follicles is plotted against the total number of predicted follicles. Initially, there is a preference for the follicles to occupy the vertices (solid blue), with also a substantial number of edge positions (open blue). After around 30 predicted follicles, the vertex positions become mostly occupied and follicles formed after that started to take on interior positions (orange.)

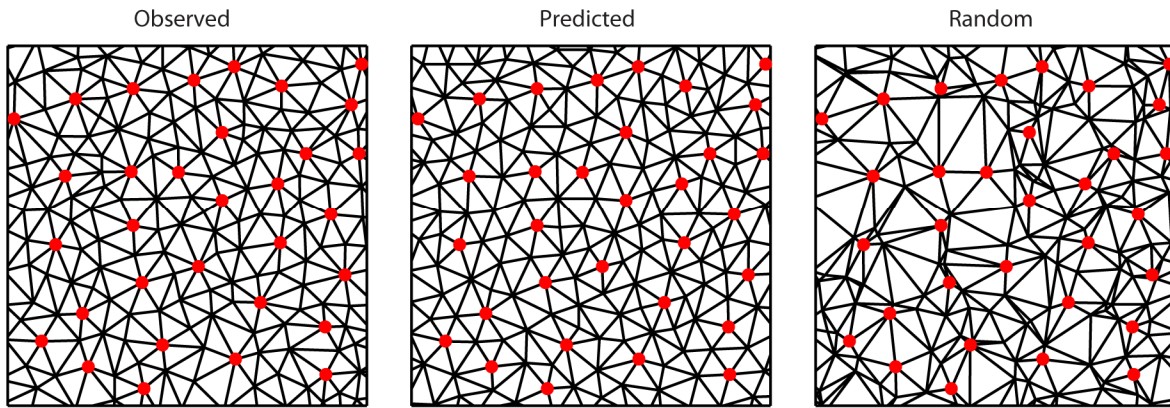


Fig. S5: The EI model reproduces the regularity of neighboring follicle distances in the skin. The locations of observed primary follicles plus observed secondary follicles (*left*), EI predicted secondary follicles (*middle*), or random secondary follicles (*right*), are used to construct Delaunay triangulations, where lines connect all neighboring follicles. Primary follicles in each case are indicated with red dots. The distribution of distances between all nearest neighbor pairs is computed from this pattern, and is observed to be sharply peaked in the observed and predicted patterns (Fig. 3C). The Delaunay triangulation also reveals the regularity in the observed and predicted follicle patterns that is not evident in the random pattern.

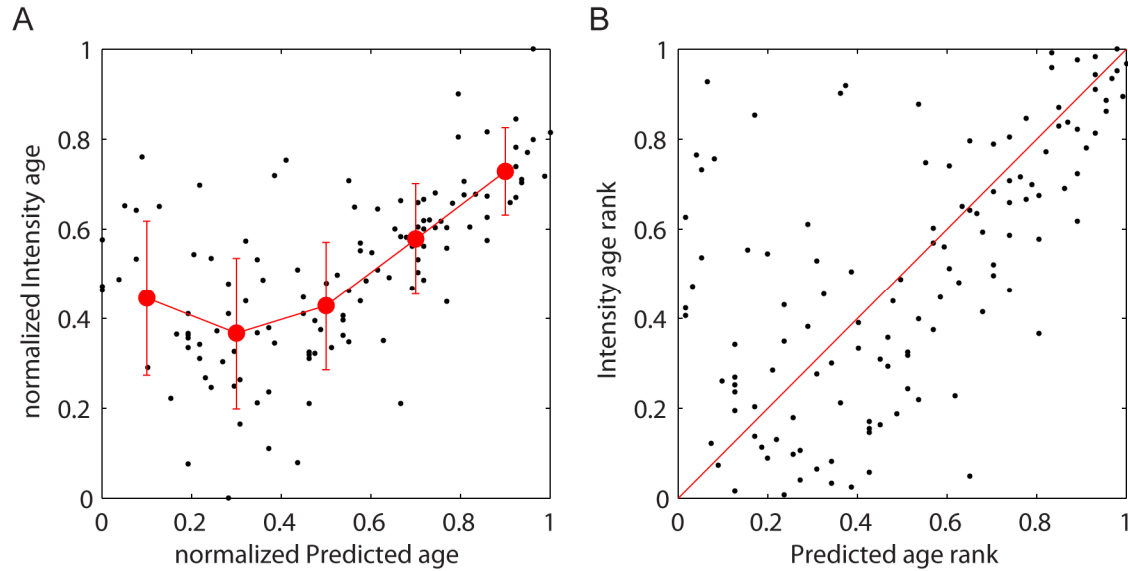


Fig. S6: Calculating the density from the rank plot of the observed age vs. the EI predicted age. (A) The intensity age of secondary follicles is plotted versus the EI predicted age for a representative sample of $Sox2^{Ysb/+}$ skin. The observed and predicted ages are clearly correlated for the oldest follicle; however, the correlation weakens for the younger (more lightly stained) follicles, due presumably to the staining characteristics (SI Appendix; Fig. S7), and differs from one image to another. (B) The rank plot for the same data in (A) shows that there is still significant noise, but the distribution is centered along the diagonal. The rank is normalized by the number of follicles observed, permitting all samples to be plotted together (as in Fig. 3D) and improving the statistics of the timing correlation. The density heat plot from Fig. 3D is calculated by 2D binning of the combined rank plot for all skin samples: we count the points in each of 10x10 bins in both directions.

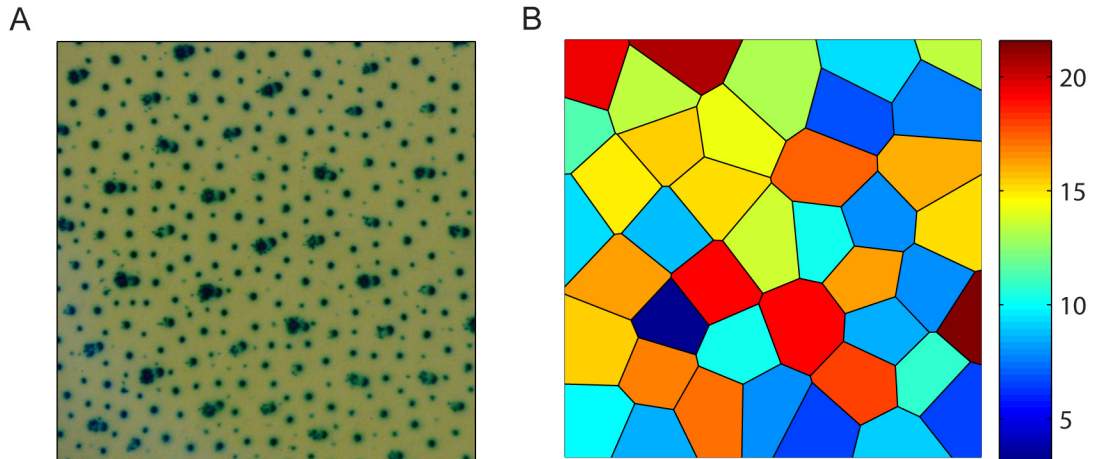


Fig. S7: The noise in the follicle age is due to heterogeneity in follicle staining.

(A) A representative image from the $Sox2^{Ysb/Ysb}$ E15.5 skins shows that there is significant variation in the follicle staining intensities, which could be due to staining or image efficiency, or other effects not accounted for in our model. (B) This variation can be seen even in the intensity of the primary follicles. We plot the Voronoi diagram for the primary follicles in (A), with the color representing the integrated intensity of each central primary follicle. The $\sim 50\%$ variation in the primary follicle intensity is similar to that of the secondary follicles and the two are not correlated (not shown).

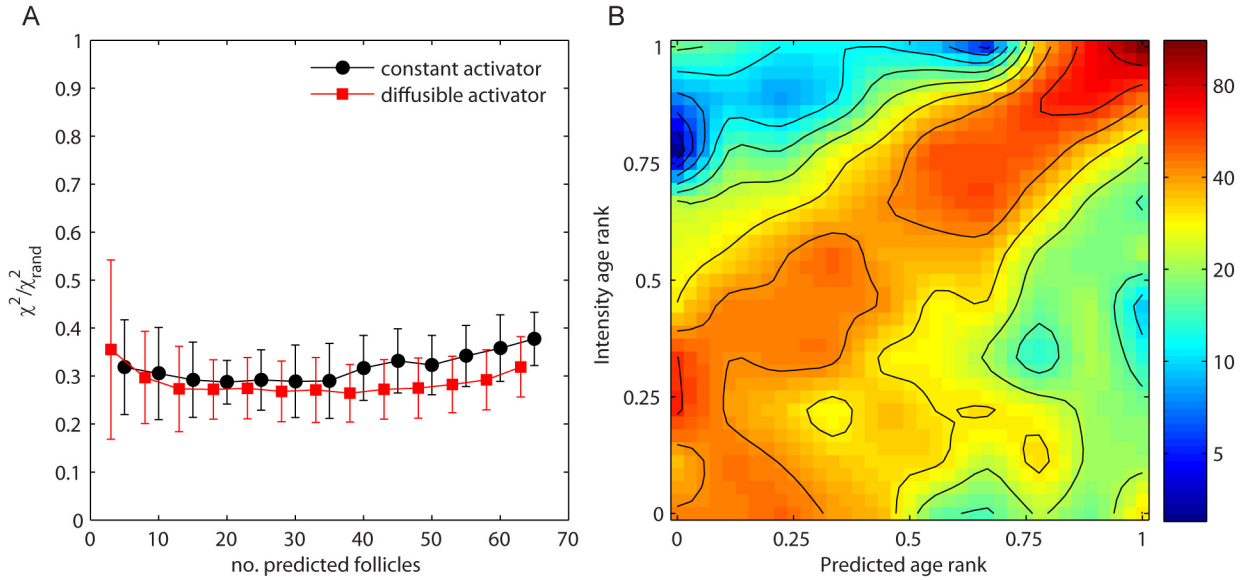


Fig. S8: The EI models with diffusible activator (red square) and basal activator (black circle) showed similar performances in predicting the process of spatial-temporal patterning of secondary hair follicles in $\text{Sox2}^{\text{Ysb/+}}$ samples ($n=10$). The Expansion-Induction model can explain the spatial patterns (A) and timing (B) of the secondary follicles using either a constant basal activation (black circles as in Fig. 3B) or a diffusible activator synthesized from the follicles (red squares). This rule holds as long as i) the activators diffuses to a longer range than the inhibitors and ii) the new hair follicles produce morphogens (activators and inhibitors) at the same rate as the existing follicles. See *SI Materials and Methods* for the details of the simulation.

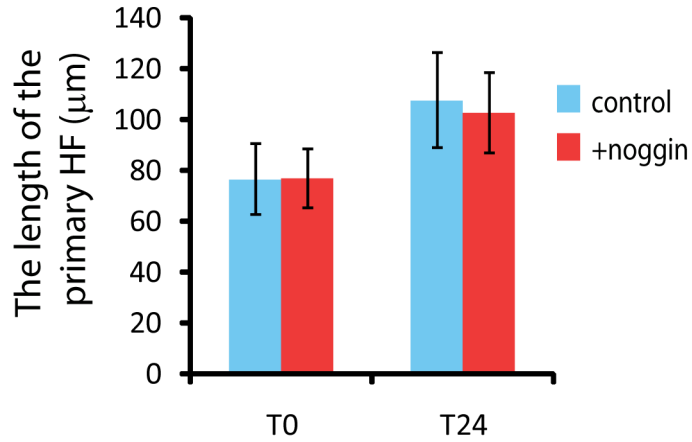


Fig. S9: Increase in vertical length of the primary hair follicle in explant culture. In explant culture experiments, the length of the hair follicles is increased after 24 hours culture, indicating the viability of the explant.

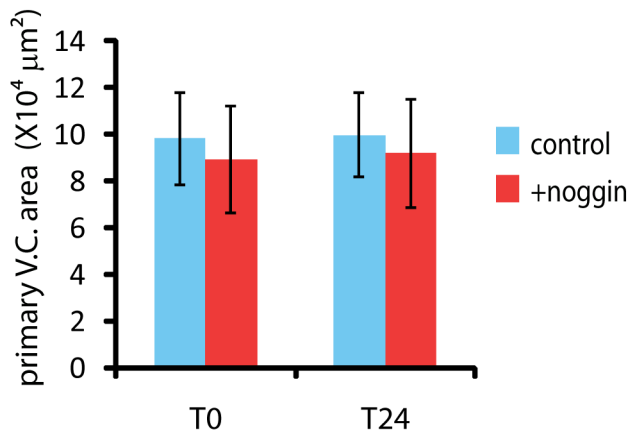


Fig. S10: No significant lateral growth of the explant during culture. The average area of the Voronoi cells generated by the primary hair follicles at the beginning of culture (T0) and after 24 hours incubation (T24). There is no significant difference between the area at T0 and T24 in both control and noggin treated samples, and suggests that is no significant lateral growth of the explant culture.

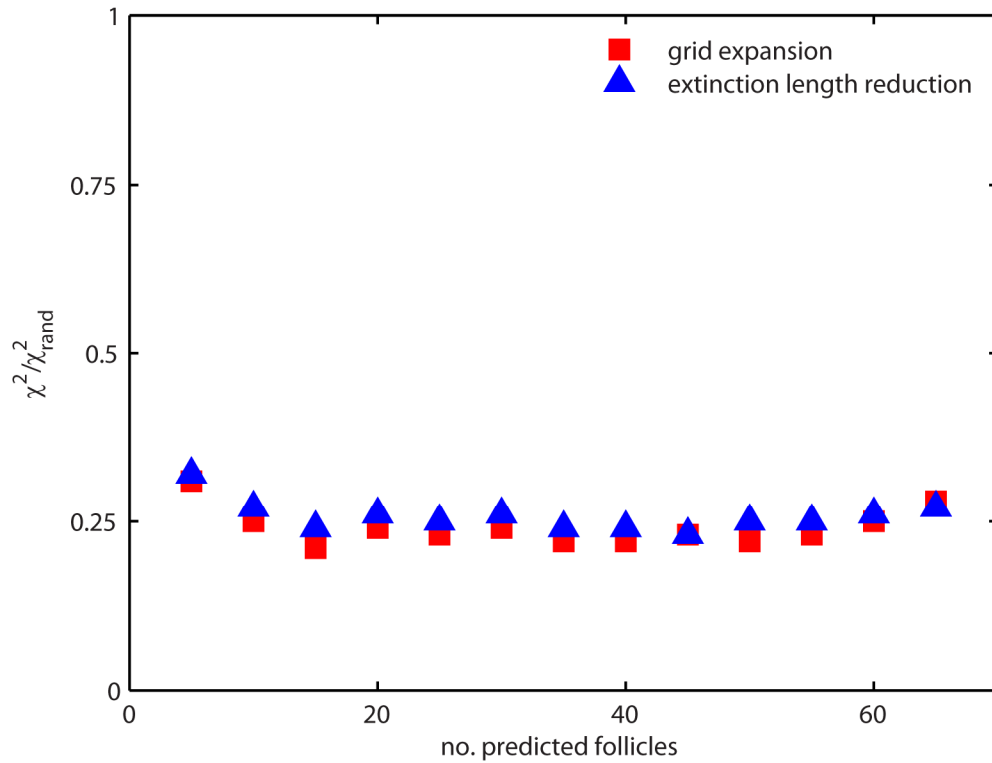


Fig. S11: Reducing the extinction coefficient of the Green's function with time is functionally equivalent to expanding the grid. The positional error of the EI predictions are plotted for a simulation using grid expansion to induce follicle formation (red), and a simulation where the follicle induction is produced by decreasing the extinction length of the Green's function with time (blue). The same primary follicle pattern is used for both simulations, and the methods produce the same accuracy of predictions. This explains why qualitatively identical follicle patterns are produced for the $Sox2^{Ysb/+}$ and the $Sox2^{Ysb/Ysb}$ skins, where follicles are induced through growth and expansion, and with noggin treated skins, where induction is assumed to result from reducing the length scale of inhibitors.

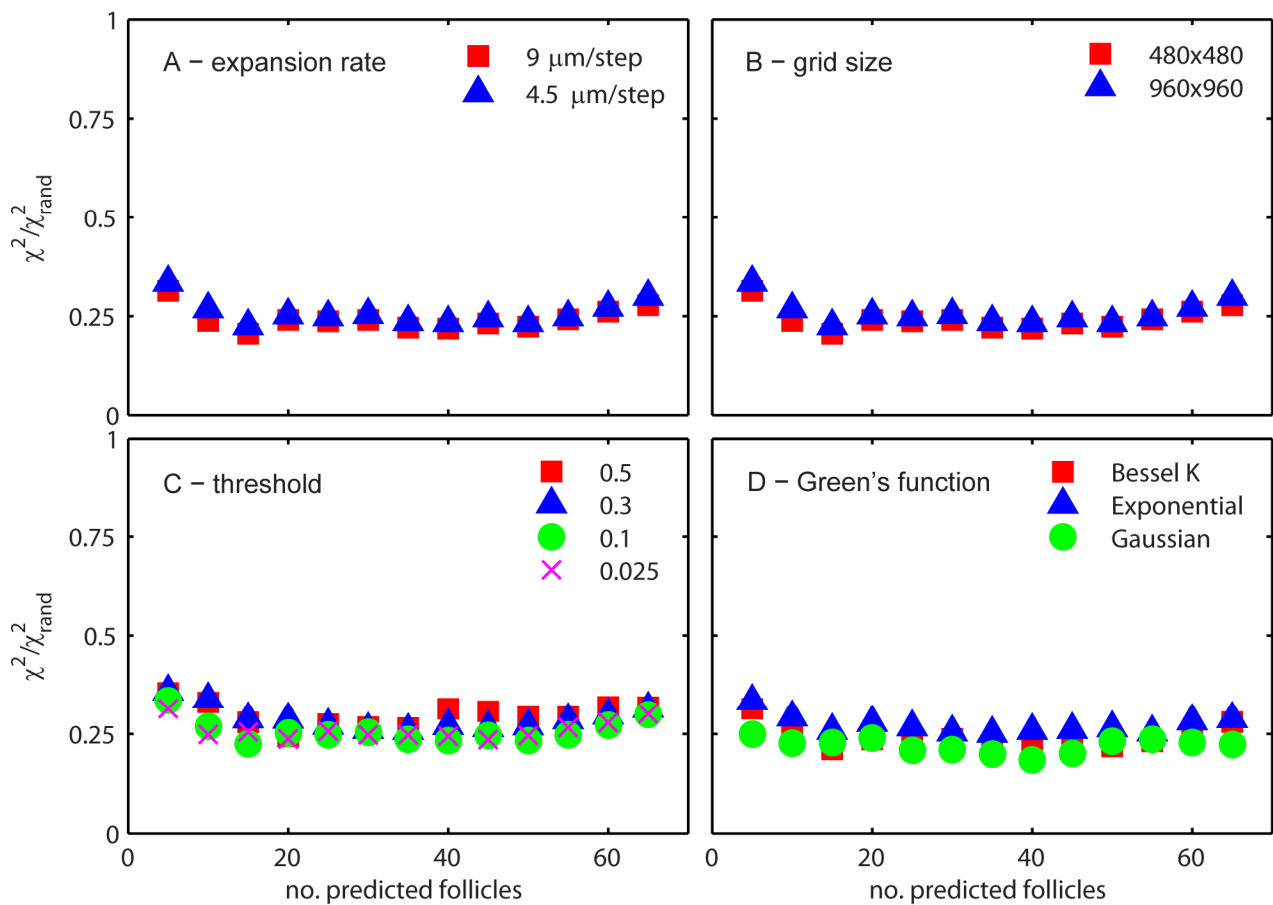


Fig. S12: The EI model predictions are robust to parameter changes. In each panel, the positional error in the predicted follicles is plotted vs. the number of predicted follicles for a representative $\text{Sox2}^{\text{Ysb/+}}$ E15.5 skin. The predictions are remarkably robust to changes in all of the relevant simulation parameters. In these simulations, expansion is accomplished through gradual reduction of the extinction length in the Green's function rather than expansion of the grid. In (A) we vary the expansion rate. The expansion rate determines the time scale (see *SI Materials and Methods*); therefore, this is equivalent to changing the time step. (B) The resolution of the image is changed two-fold. This changes the minimum length scale in the simulation. In (C) we vary the threshold level (dimensionless units), and in (D) we use different functional forms of the Green's function.

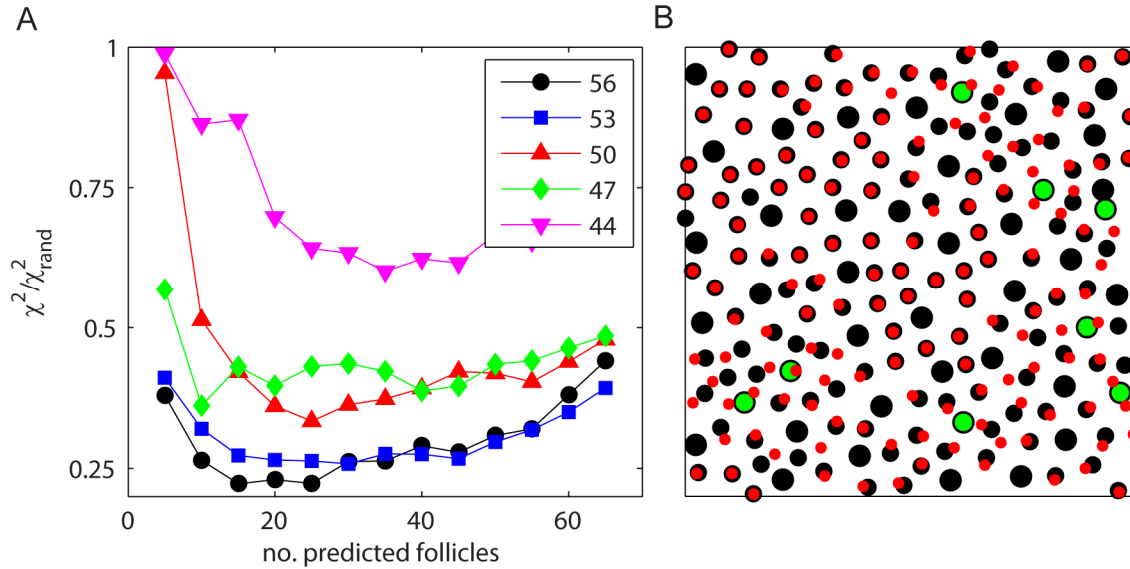


Fig. S13: Errors in initial conditions decrease the accuracy of predictions in a smooth manner. (A) The primary follicle locations are the only initial condition to the EI model. The most common problem with determining the initial condition is the misidentification of smaller primary follicles as secondary follicles. We investigate the effect of this misidentification by randomly identifying some primary follicles as secondary follicles. The positional error in the predictions is plotted versus the number of follicles predicted for different numbers of primary follicles in the initial condition (legend). The error changes smoothly with primary follicle number until 20% of the follicles are removed. (B) The positional error in the predicted pattern is localized to the region where the initial condition is missing. In this plot, the positions of the primary follicles are depicted by large black circles. Predicted secondary follicles using the complete set of primary follicles are plotted as smaller black dots. The green circles indicate primary follicles that have been removed from the initial condition in the second simulation, and red dots show the new predicted follicle locations.

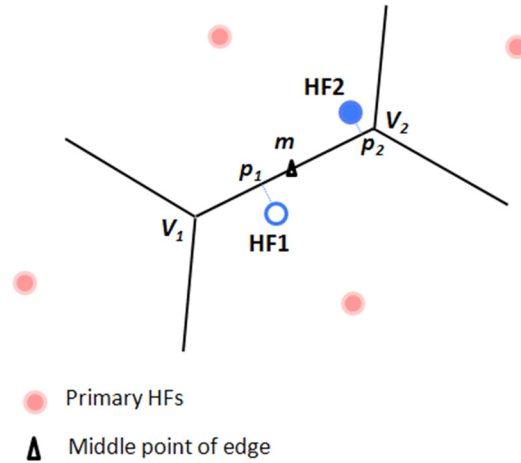
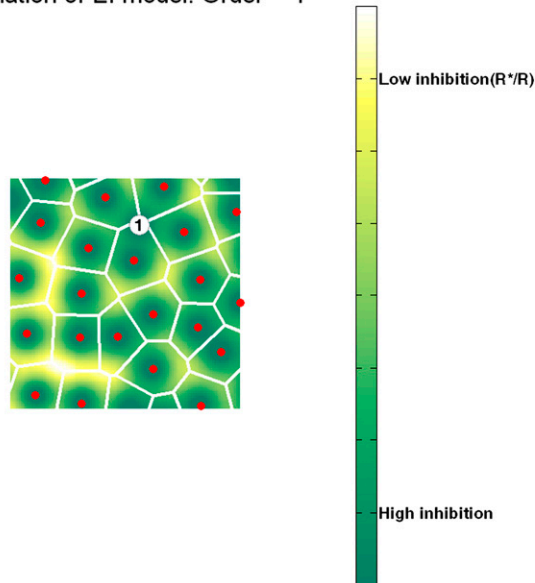


Fig. S14: Identifying the position classes of the secondary follicles. The black lines are the edges of the Voronoi diagram generated based on the positions of the primary follicles (red circles). HF_1 and HF_2 (blue circles) are two secondary follicles. p_1 and p_2 are their projections onto the closest edge $\overline{v_1v_2}$. m is the middle point of this edge. Since the ratio of distances $d(p_1, m)/d(p_1, v_1)$ is less than 1.5-fold, HF_1 is classified as a hair follicle on the edge while HF_2 is classified as a vertex HF because $d(p_2, m)/d(p_2, v_2)$ is greater than 1.5-fold.

Supporting Information

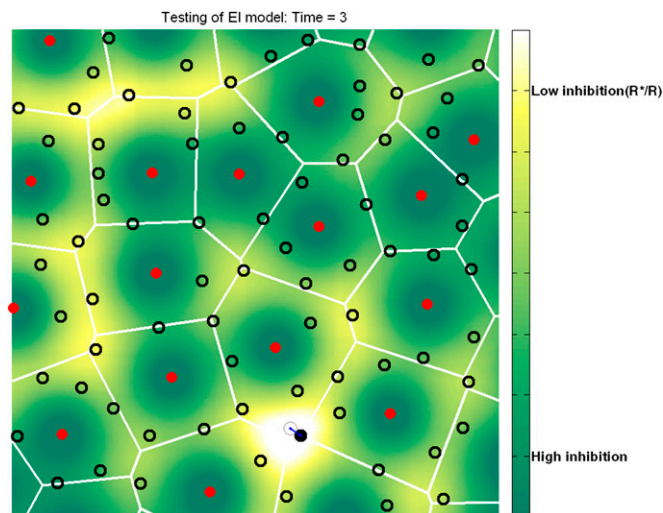
Cheng et al. 10.1073/pnas.1313083111

Simulation of EI model: Order = 1



Movie S1. This movie shows the simulation process of EI model in predicting the positions and birth time of new hair follicles. The initial condition of inhibitor was determined by the coordinates of the primary hair follicles detected in the sample image, shown as red solid circles. The lines and the solid circles in white color represented the Voronoi boundaries and the predicted hair follicles with numbers indicating their birth time. The intensity of yellow and green in the heatmap reflected the high and the low ratio of R^*/R respectively. The cross signs indicated the positions of the local minimum of inhibitor R in the grid where new follicles were to be generated as the embryo skin expanded further.

[Movie S1](#)



Movie S2. This movie shows the evaluation process of EI model in predicting the positions of secondary hair follicles. The red solid circles and the white lines indicated the locations of the primary hair follicles and the Voronoi boundaries. The black open circles represented the secondary hair follicles observed in the sample image. The white open circles indicated the predicted secondary hair follicles by using EI model. The predicted follicle was matched with an observed one if they were co-located mutual nearest neighbors. They were 'married' and shown as solid black and white circles and removed from subsequent matching procedure.

[Movie S2](#)

Other Supporting Information Files

[SI Appendix \(PDF\)](#)